

CALIFORNIA INSTITUTE OF TECHNOLOGY

DANIEL AND FLORENCE GUGGENHEIM JET PROPULSION CENTER

Kármán Laboratory of Fluid Mechanics

and Jet Propulsion

Division of Engineering

N64-19614 *

CODE-1

NASA CR-53817

SECONDARY INJECTION OF GASES

INTO A SUPERSONIC FLOW

by

Edward E. Zukoski and Frank W. Spaid

OTS PRICE	
XEROX	\$ 6.60 ph
MICROFILM	\$ 2.36 ph

Reproduced by
NATIONAL TECHNICAL
INFORMATION SERVICE
Springfield, Va. 22151

1

SECONDARY INJECTION OF GASES

INTO A SUPERSONIC FLOW

by

Edward E. Zukoski and Frank W. Spaid

N64-19614
Code - 1

Oct. 1963

70 p refs

(NASA CR - - - -) OTS:

This research work was supported by the Daniel and Florence Guggenheim Jet Propulsion Center of the California Institute of Technology and by the National Aeronautics and Space Administration, Contract No. NAS 7-100, through the Solid Rockets Section of the Jet Propulsion Laboratory, California Institute of Technology.

(NASA Contract NAS 7-100)

0547471

California Institute of Technology

Pasadena, California

1963

SUMMARY

11 19614

The flow field around the injection port for secondary injection of a gas into a supersonic stream has been studied experimentally. New information concerning pressure fields, concentration fields, and shock shapes is presented.

A scale parameter has been calculated, based on a simple, inviscid model of the flow field. This scale parameter gives a good general correlation of the data.

Use of this scale parameter allows prediction of a simple scaling law for the side forces generated by secondary injection. This side force scaling law is in approximate agreement with existing rocket motor test results.

Author

FILE FOR

TABLE OF CONTENTS

	<u>Page</u>
Summary	
Table of Contents	
List of Figures	
List of Symbols	
<u>Introduction</u>	1
<u>Description of Experiments</u>	2
<u>Description of the Flow Field</u>	4
<u>Analytic Model</u>	5
<u>Presentation of Experimental Data</u>	11
Penetration Height	11
Shock Shapes	14
Concentration Profiles	16
Wall Pressure Distribution	18
<u>Discussion and Conclusions</u>	24
Review of Flow Models	24
Review of the Flow Field Characteristics	27
Scaling Laws for Side Force on a Wall	28
References	35
Figures	37-62

List of Figures

	<u>Page</u>
1a. Sketch of the Flow Field, Turbulent Boundary Layer.	37
1b. Sketch of the Flow Field, Laminar Boundary Layer.	38
2. Penetration of Secondary Jet into Primary Flow, Nozzle Wall Data.	39
3. Penetration of Secondary Jet into Primary Flow, Flat Plate Data.	40
4. Shock Shapes, Comparison of Nozzle Wall and Flat Plate Results.	41
5. Shock Shapes Showing Mach Number Effect.	42
6a. Concentration Measurements with Argon Injection in the Plane $(y/h) = 0$, Injector Region.	43
6b. Concentration Measurements with Argon Injection in the Plane $(y/h) = 0$, Downstream Region.	44
7. Concentration Profiles in Several Planes, $(y/h) = \text{Constant}$.	45
8a. Crossplots of Argon Concentration Profiles in Planes for Which $(z/h) = \text{Constant}$.	46
8b. Concentration Contours in the Planes $(x/h) = 2.08$ and $(x/h) = 12.30$.	47
9a. Concentration Measurements with Helium Injection in the Plane $(y/h) = 0$.	48
9b. Comparison of Argon and Helium Concentration Data.	49
10. Nozzle-Wall Static Pressure Measurements in the Plane $(y/h) = 0$ at $M_{\infty} = 2.56$, with Nitrogen and Helium Injectants.	50
11a. Nozzle-Wall Static Pressure Measurements in Off-Axis Planes with Nitrogen Injection, $(y/h) = \text{Constant}$.	51
11b. Nozzle-Wall Static Pressure Measurements in Off-Axis Planes with Nitrogen Injection, $(x/h) = \text{Constant}$.	52
12. Flat-Plate Static Pressure Measurements in the Plane $(y/h) = 0$ at $M_{\infty} = 2.01$ with Nitrogen Injection. Turbulent Boundary Layer.	53
13. Flat-Plate Static Pressure Measurements in the Plane $(y/h) = 0$ at $M_{\infty} = 2.61$ with Nitrogen Injection. Turbulent Boundary Layer.	54

	<u>Page</u>
14. Flat-Plate Static Pressure Measurements in the Plane (y/h) = 0 at $M_{\infty} = 2.61$ with Nitrogen Injection. Laminar Boundary Layer.	55
15. Flat-Plate Static Pressure Measurements in the Plane (y/h) = 0 at $M_{\infty} = 3.50$ with Nitrogen Injection. Laminar Boundary Layer.	56
16. Flat-Plate Static Pressure Measurements in the Plane (y/h) = 0 at $M_{\infty} = 4.54$ with Nitrogen Injection. Laminar Boundary Layer.	57
17. Correlation of Pressure Data from Reference 6.	58
18. Variation of Side Specific Impulse with Normalized Distance from Injector to Nozzle Exit.	59
19. Correlation of Rocket-Motor Thrust Vector-Control Performance for Different Gases and Temperatures (from Reference 17).	60
20. Correlation of Rocket-Motor Thrust Vector-Control Data (from Reference 18).	61
21a. Correlation of Rocket-Motor Thrust Vector-Control Data (from Reference 15), Method of Zukoski and Spaid	62
21b. Correlation of Rocket-Motor Thrust Vector-Control Data (from Reference 19), Method of Broadwell	62

LIST OF SYMBOLS

A_j	injector area
C	discharge coefficient
C_p	pressure coefficient, $\{(P - P_\infty)/\frac{1}{2}\rho_\infty V_\infty^2\}$
d	hole diameter
D	probe diameter, see Figure 6a
F_i	force on body surface in i direction
F_j	thrust of a sonic injectant jet
F_p	total axial thrust
F_s	total side thrust
h	penetration height
I_s	effective specific impulse of injectant, F_s/m_j
K_A	mass fraction of argon
K_{He}	mass fraction of helium
M_i	Mach number
m	mass flow rate
m_i	molecular weight of i^{th} species
P	static pressure
P_o	stagnation pressure
R_i	gas constant for species (i)
Re_L	Reynolds number based on distance between leading edge of plate and injector centerline
T	static temperature
T_o	stagnation temperature
V	velocity
X	axial distance from injector port to nozzle exit

x }
 y } coordinate axes, see Figure 1
 z }

Γ function defined in equation (16)

γ_i specific heat ratio

ΔF $F_s - F_j$

ϵ ratio of nozzle area at injection station to nozzle throat area

Φ dimensionless pressure integral, defined in equation (12)

σ parameter from blast-wave theory, see References 12 and 19.

Subscripts refer to:

j and s : injectant stream

∞ and p : primary stream

Introduction

The description of the flow field set up by the injection of a secondary gas into a supersonic primary flow is a problem of current engineering interest. Flows of this type occur during thrust vector control of rocket motors, during jet reaction attitude control of vehicles moving through the atmosphere, and during fuel injection into a supersonic burner.

In all of these applications, when a gas is injected into the primary flow, a high pressure region is set up on the wall in the neighborhood of the injector. The detailed mechanism which governs the magnitude of the resulting force on the wall is not yet thoroughly understood, but may be crudely described as follows. The injected material acts as an obstruction to the primary flow and, as such, produces a strong shock wave in the primary flow. This shock interacts with the boundary layer on the wall and may cause it to separate. Both the initial shock and the resulting separation tend to produce a region of high pressure near the point of injection. A further pressure change may be produced farther downstream by mixing of the primary and secondary flows. The relative importance of the pressure fields produced by these processes has not been established and, at present, published theoretical work usually emphasizes one or the other of the processes.

The goal of the present study has been to obtain fundamental information concerning the processes of interaction which occur during secondary injection and, in particular, to determine similarity rules for the important phenomena. The situation chosen for experimental and theoretical study is the sonic injection of a gas through a wall and normal to

a primary flow which is uniform and rectilinear outside a wall boundary layer. In the present paper, a model for the interaction region is presented and is compared with experimental data obtained by the authors and by other workers.

Description of Experiments

A series of experiments were conducted in the 2.5-inch Supersonic Wind Tunnel at the California Institute of Technology in which gaseous nitrogen, argon, and helium were injected through orifices in the test-section side walls. Test section conditions consisted of Mach numbers 2.56 and 1.38 and Reynolds numbers per inch of 1.3×10^5 to 4.3×10^5 at the first Mach number and 4.5×10^5 at the second. At the Mach number of 2.56 and below a Reynolds number per inch of 1.7×10^5 , the boundary layer on the test section wall was found to be laminar; above that Reynolds number it was turbulent at the same Mach number. The tunnel could maintain quasi-steady state flow in the test section at a Mach number of 1.38 for only approximately ten seconds. It was possible to perform experiments only at a single free-stream stagnation pressure and therefore only at a single Reynolds number per inch. This Reynolds number resulted in a turbulent boundary layer in the region of the injection port.

The experimental data consisted of test-section flow conditions, schlieren photographs, static pressure distributions on the test section wall in the region of injection, concentration measurements in the flow downstream of the injection port, and the injectant total pressure and mass flow rate. The static pressures were measured by mercury

manometers, and the concentration measurements were obtained with a Gow-Mac thermal conductivity cell.

In addition to the experiments at the California Institute of Technology, experiments were conducted in the 20-inch Supersonic Wind Tunnel at the Jet Propulsion Laboratory. These experiments were part of a series conducted by J. F. Newton, Jr. and M. W. Dowdy. (1)* Gaseous nitrogen was injected through a sonic orifice 0.100 in. in diameter normal to the surface of a sharp-edged flat plate, 7.00 in. to the rear of the leading edge. The surface of the plate in which the injector was located was parallel to the test section flow, and a boundary-layer trip wire was attached near the leading edge of the plate. Tests were conducted at test-section Mach numbers of 4.54, 3.50, 2.61, and 2.01. The highest and the lowest practical tunnel stagnation pressures were utilized at each Mach number except 3.50 in an attempt to study the effect of test-section Reynolds number at a fixed Mach number, but only at Mach 2.61 was it possible to achieve both laminar and turbulent boundary layers, at Reynolds numbers based upon the distance from the injection port to the leading edge of 0.749×10^6 and 1.99×10^6 , respectively. At Mach numbers 4.54 and 3.50, the boundary layer on the plate near the injection port was always laminar; and at Mach number 2.01, it was always turbulent.

The experimental data consisted of schlieren and shadowgraph pictures, tunnel and injection conditions, and static pressure measurements on the plate in the injection region. The static pressures were measured by a single transducer and a pressure-switching mechanism.

* Numbers in parentheses refer to references listed at the end of the paper.

Description of the Flow Field

A crude picture of the flow field produced by injection through an orifice has been obtained by examination of schlieren and shadowgraph pictures of the interaction region. Figures 1a and 1b are scale drawings of two shadowgraph pictures taken at different free-stream stagnation pressures but at the same ratio of jet stagnation pressure to free-stream stagnation pressure. The free-stream Mach number was 2.61 and the flat plate model was used here. For these examples, the injected material enters, through a circular orifice, with a static pressure much higher than the value in the undisturbed primary flow. The flow is sonic at the injector and expands rapidly through a strong Prandtl-Meyer fan. The interaction of the two streams produces a strong bow wave on the upstream side of the injector, and the shock-induced pressure field turns the injectant so that it moves approximately parallel to the wall.

The bow shock wave - boundary layer interaction produces a region of boundary layer separation upstream of the shock. For the case of a turbulent boundary layer, the example illustrated in Figure 1a, the separated region is short, and the oblique shock produced by separation is often too weak to be observed. When the boundary layer is laminar, Figure 1b, the separated region is much larger, and the angle between the separated flow and the wall is never more than a few degrees.

Some details of the flow near the injector are shown on the schlieren photographs. One feature which is usually seen, and which is apparently the region of maximum concentration of the injectant, has the appearance of a streamline of the injectant. Determination of the maximum distance between this feature and the wall (see Figure 1)

gives a simple visual measure of the penetration of the secondary fluid into the primary flow. Figures 1a and 1b illustrate flow conditions in which the distance of this feature from the wall is much larger than a characteristic boundary layer dimension.

Shadowgraph pictures taken at the higher Mach numbers and correspondingly lower test-section Reynolds numbers showed wavy shocks and jet outlines, which indicated unsteady flow. This unsteady behavior has also been reported by Amick and Hayes⁽²⁾.

Analytic Model

In investigating the shock patterns produced by secondary injection, one is reminded of shock shapes produced by blunt axisymmetric bodies. This fact suggested that some insight into the scaling laws for secondary injection could be obtained by setting up a simple model for a solid body which would give a shock pattern similar to that produced by the injectant. For the purposes of this simple model, it is assumed: (1) that a sonic jet is injected into a uniform supersonic flow with no wall boundary layer; (2) that no mixing occurs between the two flows; (3) that the interface between the flows is a quarter sphere followed by an axisymmetric half body; (4) that pressure forces on the sphere can be calculated by use of modified Newtonian flow; and (5) that the injectant expands isentropically to the ambient pressure with the vector parallel to the wall at the downstream face of the sphere.

Assumption (4) is not as restrictive as the derivation of Newtonian flow equations implies. Although the Newtonian approximation is a limiting process in which $M_{\infty} \rightarrow \infty$ and $\gamma_{\infty} \rightarrow 1$, comparison with

experiment has shown that the pressure distributions on the upstream sides of blunt bodies are predicted reasonably well by Newtonian flow calculations over a wide range of Mach numbers, and for $\gamma_{\infty} = 1.4$.⁽³⁾

The coordinate system used in the analysis and in the description of the experiments is illustrated in Figure 1. The x-z plane is shown here with the y-axis perpendicular to the page. The origin of the coordinate system has been chosen so that the $y = 0$ plane includes the center of the injector and so that the origin of the coordinate system lies at the intersection of the bow shock wave with the wall.

In this model, everything is determined except the scale of the body given by the radius, h , of the quarter sphere. This radius is found by equating (1), the x-component of the pressure force acting on the spherical surface due to the primary flow to (2), the change in x-component of momentum of the injected gas as it is turned through a right angle. Note that the injectant is allowed to expand to the static pressure of the undisturbed flow, but is not assumed to completely fill the semicircular cross section of the downstream face of the quarter sphere which forms the "nose" of the equivalent solid body. The mass flow of injectant is calculated from the assumption that the injector flow is sonic and fills an area which is c times the actual injector area; that is, c is a discharge coefficient for the injector and $\{\sqrt{c} d\}$ is the equivalent diameter of the injector, and hence is the characteristic dimension of the injector.

A brief description of the derivation of the equation for the penetration height is given here. First, consider the flow over the spherical nose. For Newtonian flow calculations, with the modification suggested by Lees⁽⁴⁾, the pressure coefficient, $C_p \equiv (P - P_{\infty}) / \frac{1}{2} \rho_{\infty} V_{\infty}^2$, on the

surface of a body is given by

$$\frac{C_p}{C_p^*} = \frac{\sin^2 \alpha}{\sin^2 \alpha^*}$$

where α is the angle between the local tangent to the surface and the undisturbed flow direction, and must lie between 0 and $\pi/2$. Here, C_p^* and α^* are evaluated at the nose of the body. Hence, $\alpha^* = \pi/2$ and C_p^* is the pressure coefficient corresponding to the stagnation pressure behind a normal shock, found from the theory of supersonic flow of an ideal gas:

$$C_p^* = \frac{2}{\gamma_\infty M_\infty^2} \left[\left(\frac{\gamma_\infty + 1}{2} M_\infty^2 \right)^{\frac{\gamma_\infty}{\gamma_\infty - 1}} \left(\frac{\gamma_\infty + 1}{2\gamma_\infty M_\infty^2 - \gamma_\infty + 1} \right)^{\frac{1}{\gamma_\infty - 1}} - 1 \right] \quad (1)$$

In this case, the Newtonian calculation is applicable only to the surface of the quarter sphere. The total axial force on the spherical surface was obtained by integrating the pressure force in the x-direction over the spherically-shaped nose of the equivalent body. The result is:

$$F_x = \frac{\pi}{8} M_\infty^2 \gamma_\infty C_p^* h^2 P_\infty \quad (2)$$

The force on the inside surface of the nose is found by making a momentum balance of the injectant flowing through a control volume whose surfaces are made up of (1) the spherically shaped nose, (2) the side wall lying under the nose, and (3) the portion of the $x = \text{constant}$ plane lying just downstream of the nose. The x-component of the momentum change in the jet is equal to the force on the nose since the x-component of force can only act on the injectant. Because the jet is injected normal to the wall, the momentum change is equal to the total x-momentum of the injected gas after it has expanded isentropically to the local ambient pressure.

This momentum flux can be simply evaluated. First, the mass flux of the injectant is equal to the mass flux at the injector port. From the assumption of sonic flow at the injector, it follows that:

$$\dot{m}_j = cA_j P_{o_j} \left[\left(\frac{\gamma_j}{R_j T_{o_j}} \right) \left(\frac{2}{\gamma_j + 1} \right)^{(\gamma_j + 1)/(\gamma_j - 1)} \right]^{\frac{1}{2}} \quad (3)$$

where (cA_j) is the equivalent injector area. The Mach number at the exit of the control volume is given by the expression for isentropic expansion from a stagnation pressure P_{o_j} to a static pressure P_{∞} . This expression can be solved for the velocity, V_j , and the result is

$$V_j = \left[\left(\frac{2\gamma_j R_j T_{o_j}}{\gamma_j - 1} \right) \left\{ 1 - \left(\frac{P_{\infty}}{P_{o_j}} \right)^{(\gamma_j - 1)/\gamma_j} \right\} \right]^{\frac{1}{2}} \quad (4)$$

The momentum flux is just $\dot{m}_j V_j$, and consequently, the force balance is then given by

$$F_x = \dot{m}_j V_j \quad (5)$$

All the parameters in this equation are known except the penetration height, and therefore, equation (5) can be solved for this parameter. The result is:

$$\frac{h}{d\sqrt{c}} = \left\{ \left(\frac{1}{M_{\infty}} \right) \left(\frac{P_{o_j}}{P_{\infty}} \frac{\gamma_j}{\gamma_{\infty}} \frac{2}{C_p} \right)^{\frac{1}{2}} \times \left[\frac{2}{\gamma_j - 1} \left(\frac{2}{\gamma_j + 1} \right)^{(\gamma_j + 1)/(\gamma_j - 1)} \left(1 - \left(\frac{P_{\infty}}{P_{o_j}} \right)^{(\gamma_j - 1)/\gamma_j} \right) \right]^{1/4} \right\} \quad (6)$$

A similar analysis can be carried out for momentum change in the y-direction. The resulting equation is quite similar functionally and gives numerical values which are only very slightly lower than those obtained from equation (6).

Note that when the ratio (P_{o_j}/P_{o_∞}) is held fixed, the penetration height decreases with increasing Mach number. However, for rocket work, it is often more convenient to use the stagnation pressure ratio, P_{o_j}/P_{o_∞} , as the independent variable.

The first two factors of (6) may be rewritten to give:

$$\left\{ \frac{1}{M_\infty} \left(1 + \frac{\gamma_\infty - 1}{2} M_\infty^2 \right)^{(\gamma_\infty)/2(\gamma_\infty - 1)} \left(\frac{P_{o_j}}{P_{o_\infty}} \frac{\gamma_j}{\gamma_\infty} \frac{2}{C_p^*} \right)^{\frac{1}{2}} \right\}. \quad (7)$$

It is evident from this form of these terms that the penetration height increases with the square root of P_{o_j}/P_{o_∞} and, in a more complex manner, with M .

The variations of the terms in the square bracket of equation (6) and that of C_p^* with M_∞ or γ_∞ are not very rapid. Hence, the most important variation of penetration height is approximately given by:

$$h \propto (d\sqrt{c}) \left(\frac{1}{M_\infty} \right) \left(\sqrt{\frac{P_{o_j}}{P_{o_\infty}}} \right). \quad (8)$$

In terms of the mass flow rate of injectant, \dot{m}_j , equation (8) can be written as

$$h \propto \frac{1}{M_\infty} \sqrt{\frac{\dot{m}_j}{P_{o_\infty}}} \left(R_j T_{o_j} \right)^{1/4}. \quad (9)$$

Note that for simplicity, the complex dependence on γ_j and γ_∞ has been omitted here. Equations (8) and (9) are useful as long as

$(P_{o_\infty}/P_{o_j}) \ll 1$ and $M_\infty > 2$.

Although the derivation used to obtain equation (6) was based on the assumption of a spherical interface between primary and injectant flows, it should be noted that the functional form of equation (6) is not sensitive to the shape of the interface. For example, the derivation has

been carried out for elliptical interface shapes with eccentricities ranging between 0 and 0.98 . The equations for h obtained by this calculation had the same functional form given in equation (6) and differed from it by a multiplicative constant which depended on the eccentricity and which only changed by a factor of 2.3 for the range of eccentricities given above.

It is proposed that the penetration height can be used as a measure of the scale of the disturbance produced by injection. Note that although the expression for h , given in equation (6), contains no adjustable constants , the exact correspondence between values calculated from equation (6) and any measured feature of the flow, such as the penetration height mentioned earlier, is purely fortuitous. However, it is to be expected that changes in scale of flow features will be proportional to changes in h .

Since the boundary layer has not been considered at all in this analysis, it would be expected that h would have to be much larger than a characteristic boundary layer dimension in the immediate vicinity of the jet, i. e., a characteristic thickness of the boundary layer in the region of maximum separation, in order for the analysis to be applicable.

However, there is a difference between the observed flow field and the model which seems to make this limitation somewhat less severe. As the injectant expands just after leaving the orifice, it is initially conical in shape so that the actual obstruction shape as viewed from the front is probably similar to that of a frustrum of a cone with its small end resting on the wall, and capped by a sphere. This shape would be expected to produce considerably less of an obstacle to the boundary layer than a quarter sphere of the same projected area.

Figures 1a and 1b give typical examples of the change in boundary layer thickness caused by injection. The maximum thickness of the separated boundary layer was never observed to be more than about twice the thickness of the undisturbed boundary layer at the same distance from the plate, as determined from the photographs.

To provide a basis for comparison, some experiments with solid objects of the same shape as that postulated in the analytic model have been conducted. These objects were attached to the nozzle wall, and schlieren pictures were taken at a test-section Mach number of 2.56. Photographs with the same shock shape were compared. The separation produced with both laminar and turbulent wall boundary layers was always considerably more extensive than that produced by injection, thus verifying the previous supposition about the applicability of the model.

Presentation of Experimental Data

In the following sections, results are given of experiments concerning the flow field geometry, concentration measurements, and static pressure measurements on the wall. The data are presented in terms of space coordinates normalized by the penetration height, which is calculated from equation (6). This mode of presentation was used to facilitate the verification of the proposed scaling law.

Penetration Height. In most of the schlieren photographs taken with secondary injection of argon and nitrogen into air, a distinct feature appears which looks like the top or outer boundary of the jet. Although this feature, shown in Figure 1, is probably the line of maximum concentration of injectant rather than the jet boundary, it has been selected as being characteristic of the scale of the disturbance produced by the jet,

and hence is called the penetration height of the jet. That flow fields for different injection rates should be geometrically similar is, of course, an assumption which must be verified.

Values of the penetration heights determined directly from schlieren photographs made in the CIT facility are shown in Figure 2. Here, penetration heights normalized by the equivalent injector diameter, $(\sqrt{C} d)$, are given as a function of the ratio of injectant to primary stream stagnation pressures; data are presented for two Mach numbers. Nitrogen and argon were used as injectants, and experiments were conducted with two injector diameters.

The magnitude of the penetration height was found to depend directly on the equivalent injector diameter and to vary approximately with the square root of the injector - to - primary flow stagnation pressure ratio. No dependence on injector molecular weight or specific heat ratio was noticed when penetration heights for a given total pressure ratio were compared.

The data shown in Figure 2 were obtained with laminar and turbulent boundary layers. It is particularly interesting to note that measured values of the penetration height were not noticeably dependent on the state of the boundary layer.

The data of Figure 2 show that the height increases with increasing Mach number in the primary stream. This is a result of the fact that for a given primary stream stagnation pressure, the local static pressure decreases rapidly with increasing Mach number.

Theoretical values of penetration heights are also shown in Figure 2 for both Mach numbers. The agreement between experiment and theory is good over the whole pressure ratio range studied, and the dependence

on specific heat ratio, molecular weight, and Mach number is correctly predicted.

Values of penetration heights were obtained in the JPL facility from shadowgraph photographs for a wide range of Mach number and pressure ratio. Comparison of these data with that obtained in the CIT facility showed that the JPL, flat plate results were about 20 per cent lower than the comparable CIT, nozzle wall data. This systematic difference is probably due to the fact that shadowgraphs were used in one case and schlieren photographs in the other. (The different optical techniques naturally lead to slightly different heights because the schlieren system is sensitive to density gradients, whereas the shadowgraph system is sensitive to the curvature of the density.) Also, in comparing the data with the results predicted from the model, it should be remembered that the features examined on either schlieren or shadowgraph pictures are not the jet boundaries themselves, and hence that either the calculated or the measured penetration heights can only be viewed as being proportional to the actual characteristic scale of flow.

Comparison of the flat plate data and the results of equation (6) are shown in Figure 3. Here, all of the measured penetration heights are increased by 20 per cent. The agreement between theory and experiment appears to be good, although the experimental data may have a slightly more rapid variation with Mach number than is predicted from equation (6).

Although the good absolute agreement between the prediction of equation (6) and measured values is fortuitous, the fact that the data agree so well in slope and shape over a range of injector diameter, injection pressure, and primary-flow Mach number indicates that the value of the

penetration height predicted by equation (6) is a useful measure of the scale of the interaction phenomena and suggests that the proposed model does include the pertinent physical phenomena. The success of this simple model in predicting the penetration heights also indicates that the gross features of the flow field can be characterized by a single dimension which is proportional to h .

Shock Shapes. As a further check on the suggestion that h is a characteristic dimension of the flow field, the shapes of the bow shock waves, as seen from the side, were determined from schlieren and shadowgraph pictures from both the flat plate and nozzle wall data. In all cases, the shock coordinates were normalized by values of h calculated from equation (6). In Figure 4, a few typical cases from the nozzle wall data are compared. The shock shapes plotted here cover the maximum range of parameters studied in the CIT Supersonic Wind Tunnel, and are typical of the measurements made of more than 50 schlieren photographs. In addition, the solid line in Figure 4 represents the average of the data which were obtained from the flat plate experiments at a Mach number of 2.61. These data showed somewhat less scatter than did the nozzle wall data which are plotted here.

It is again evident from study of these data that the normalized coordinates agree well and that the agreement appears to be independent of pressure ratio, specific heat ratio, injector diameter, and the condition of the boundary layer. In addition, the fact that the data from schlieren and shadowgraph pictures agree well substantiates the assertion that the observed differences in penetration height from these sources is a result of the differences between these two flow visualization techniques.

In order to check the influence of molecular weight on the process, some shock shape data were obtained with helium injectant. Unfortunately, schlieren photographs taken with helium did not reveal the penetration distance directly, although the bow shock was easily observed. However, the normalized shock shapes agree as well as the other data when the data are normalized by values of penetration height calculated from equation (6) with experimentally determined values of the flow coefficient, c . Hence it is evident that the characteristic dimension of the interaction is independent of molecular weight.

In Figure 5 are presented curves which represent averages of shock shape data from the JPL flat plate experiments. This method of data presentation was chosen because the curves lie so close together that it would have been very difficult to visualize the important features had the data points been plotted, but yet their significance is lost if they are not directly compared. The scatter in the data is somewhat less than that shown in Figure 4 except where the curves are dashed, in which case the difficulty in interpreting the photographs caused greater scatter. Some of this difficulty at the higher Mach numbers was caused by the unsteadiness in the flow field previously mentioned. The fact that the curves all approach a single curve for small values of (x/h) indicates that the properly normalized shock shapes near the injector port are nearly identical. Now the shock location near the nose of a blunt body in a supersonic flow is very weakly dependent on Mach number (for Mach numbers larger than about 2.0), but is strongly dependent upon the size of the body. Thus, Figure 5 indicates that the dependence of h upon the free-stream Mach number is correctly predicted by equation (6).

Concentration Profiles. A more critical check on the proposed scaling law is given by examination of the flow pattern of the injectant. The mixing of the injectant and primary flows has been examined by making analyses of gas samples drawn from various locations in the flow field. Measurements were taken at Mach number 2.56 in the nozzle-wall injection system with argon and helium injectants. The positions most thoroughly studied lie in the x - z plane, $y = 0$; a few positions for other values of y were also examined.

Data obtained with argon injectant in the $y = 0$ plane are shown in Figures 6a and 6b. Here, the origin of each concentration profile is superimposed at the appropriate position on a plot of the x - z plane which also shows the bow shock wave. In Figure 6a, the region close to the injector is shown on an expanded scale, and the data points are presented in detail to illustrate the reproducibility of the experiments. All coordinates are normalized by calculated values of the penetration height. The probe which was used to obtain these concentration measurements was 0.079 cm outside diameter. The normalized diameter of the probe is shown in Figure 6a for each value of h used in the experiments.

The data of Figure 6 show that near the injector the profile is sharply curved on the lower side of the maximum, but that downstream of $(x/h) \approx 4$, the profile is roughly Gaussian except for a slight wall interference effect. It is obvious that the observed and calculated penetration height correspond much closer to the line of maximum concentration than to the outer edge of the injectant stream.

Mixing occurs rapidly close to the injector. For $(x/h) \approx 1$, the maximum concentration is less than 0.80; thus, even this close to the injector, the injectant is already substantially mixed with the primary flow.

Farther downstream mixing is slower, and at $(x/h) \approx 12$ the concentration maximum is still greater than 25 per cent.

Measurements made on planes other than $y = 0$ are shown in Figure 7 for two values of (x/h) . These data and that shown in Figure 6 have been used to obtain the cross plots and concentration profiles shown in Figures 8a and 8b. In Figure 8a, cross plots of concentration versus (y/h) for a number of values of distance above the wall, (z/h) , and for two values of (x/h) are shown. Above the concentration maximum, the curves are again roughly Gaussian, but below it they have a definite concentration minimum on the $(y/h) = 0$ axis. This minimum is present at both (x/h) stations, but is much less marked at $(x/h) = 12$.

The concentration profile of Figure 8b shows the extent of this minimum more clearly. Here lines of constant concentration in the $(y/h) - (z/h)$ plane are presented. The solid points shown on the figure were obtained by interpolation of the data of Figures 6 and 7. The shapes of the two plots are roughly similar, although the (x/h) dimension appears to be growing slightly more rapidly than the (y/h) dimension.

The kidney-shaped cross section seen in the concentration profiles of Figure 8b suggests that a vortex is shed from either side of the injectant jet. The vortex filaments appear to be roughly parallel to the wall, and with vorticity such that, near the wall, primary gas is swept in toward the centerline of the flow, i. e., toward $(y/h) = 0$. This type of vortex structure has been observed by other workers for the case of subsonic injection into a subsonic stream.⁽⁵⁾ Such vortices may explain the steep gradients in concentration observed at the $(x/h) \approx 2$ position.

The data presented in the last three figures were obtained with argon injectant. Similar data obtained with helium injectant are shown in

Figure 9a. As would be expected, these curves, presented in terms of mass fractions, are not identical with the argon data, since the two situations are not directly comparable. The difference becomes more marked with increasing (x/h) . The nature of the difference is more clearly shown in Figure 9b, where the profiles for helium and argon at $(x/h) = 12.3$ are compared with the concentration values normalized by the maximum value. The curves are similar, but the helium profile is lower than that for argon.

Although the general shapes of the curves shown in Figures 9a and 9b are quite similar, such features as jet width and distance of maximum concentration line from the wall are definitely smaller for the helium case. Hence, in the coordinates used here, the helium jet spreads more slowly than the argon jet.

Argon data are presented in Figures 6 to 8 for stagnation pressure ratios which give a 2.2:1 change in penetration height. The normalized concentration profiles shown in these figures are almost identical over this scale change. The data are also insensitive to the state of the boundary layer, since both laminar and turbulent layers are included. Hence, it is apparent that the scaling rule given by equation (6) is valid for the mixing process, too, when changes in scale by not more than a factor of two are considered; the good agreement of the data suggests that much larger scale changes could be adequately treated.

Wall Pressure Distribution. The experimental results discussed up to this point concern the gross structure of the flow field produced by secondary injection. It has been shown that these features of the flow are approximately independent of the state of the boundary layer, and that a simple model of the flow leads to the calculation of a single characteristic

dimension, the penetration height, which is a satisfactory scaling parameter. In contrast, when examining the flow field near the wall, the state of the boundary layer is very important because of its influence on the interaction between the bow shock and the boundary layer.

For example, when the layer is laminar, the bow shock - boundary layer interaction causes the layer to separate far upstream of the interaction region, and the separation angle is quite small, e.g., Figure 1b. When the layer is turbulent, the separation point is much closer to the interaction region, and the separation angle is much larger (Figure 1a). Hence, it is evident that the static pressure distribution on the wall under the separated regions will be quite different for turbulent and laminar boundary layers.

Static pressure data obtained in the CIT and JPL facilities are shown in Figures 10 through 16. Values of the pressure change produced by injection and normalized by the primary flow static pressure are given as a function of the position coordinates normalized by the calculated penetration height.

Consider first the results for $M = 2.56$ shown in Figures 10 and 11. In Figure 10, data are shown for pressures measured along the x-axis, i. e., along a line parallel to the primary flow and passing through the injector port. In general, the pressure increases rapidly between $-1 \leq (x/h) \leq -\frac{1}{2}$ on the upstream side of the injector port, falls to less than half the ambient around the port, and rises to the ambient value in the region $3 \leq (x/h) \leq 4$. When the boundary layer is laminar, the pressure increases slightly farther upstream of the shock due to separation; the corresponding turbulent separation occurs too close to the injector to be clearly discerned.

Off x-axis data are shown in Figure 11 for conditions corresponding to the turbulent boundary layer data of Figure 10. The data are for cuts along both $y = \text{constant}$ and $x = \text{constant}$ lines and serve to give a rough picture of the off-axis pressure distribution. As would be expected, pressure extremes are found along the x-axis and die off with distance away from this axis.

A wide range of injector parameters are covered by the data presented in Figures 10 and 11. For example, the change in total pressure ratios used here produces a 6.8:1 variation in the penetration height; data with both laminar and turbulent boundary layers are presented, and helium and nitrogen injectants are used. In view of this wide variation of parameters, the correlation of the data of Figures 10 and 11 by use of the normalization factor, h , is satisfactory.

The pressure distributions obtained at different Mach numbers for the flat plate model are shown in Figures 12 through 16. Again, it was not possible to present all of the data points; each figure includes one set of data points, and the scatter in the data for which only average curves are given is similar to that of the data which are presented.

At the lowest Mach numbers, the pressure distributions were obtained with turbulent boundary layers, and the data are in good qualitative agreement with the nozzle wall data of Figure 10. A curve representing the average of the CIT data of Figure 10 is given in Figure 13 to facilitate this comparison. One of the differences between the nozzle wall and the flat plate data for the case of turbulent boundary layers was that separation could usually be observed in the flat-plate pressure distribution data. In the cases for which the separation shock was visible in the shadow-graph pictures, the point at which the pressure rise was detected cor-

responded reasonably well with the intersection of the separation shock with the wall.

Data with laminar boundary layers are shown in Figures 14, 15, and 16 for the higher Mach numbers. These data show a much more pronounced pressure rise far upstream of the injector than the corresponding turbulent data; for example, compare data of Figures 13 and 14 which were obtained at Mach number 2.61 and which have similar scale heights. Downstream of the injector, the data are similar for both boundary layer states. In general, the normalized pressure distributions with either a laminar or a turbulent Mach number are surprisingly insensitive to Mach number.

In spite of the good general correlation of the pressure data in Figures 12 through 16, some systematic variations with pressure ratio, or scale, can be noted. In the case of laminar separation, Figures 14 to 16, it can be seen that the separation distance normalized by h decreases as h increases. Considering the assumptions of the analytic model, it is not surprising that it does not account for an effect of shock - boundary layer interaction particularly well. However, in the case of the turbulent boundary-layer data upstream of the injector, the correlation is excellent, and thus it appears that the turbulent separation distance is a linear function of h .

In Figures 12 through 16 it can be seen that the agreement in the data is very good immediately downstream of the injection orifice in the region of minimum pressure, but a systematic difference appears somewhat farther downstream, in the range of (x/h) between 3 and 5. As h , or the injection pressure, increases, the pressure in this region rises

more abruptly, until it actually overshoots the free-stream static pressure except at Mach number 4.54. At the lower Mach numbers, this overshoot becomes more pronounced, and its maximum value moves forward, in the normalized coordinates, as the injection pressure is increased. This overshoot occurs considerably downstream of any visible feature in the shadowgraph pictures to which it might be attributed.

This pressure overshoot is probably caused by the reattachment of the injectant jet to the wall. The increase in overshoot pressure with penetration height is explained by the fact that h is increased by increasing the total pressure, P_{o_j} . As h increases, the pressure ratio through which the injectant expands, i. e., P_{o_j}/P_∞ , increases, and the velocity in the jet must increase. Hence, the turning shock must be stronger and the pressures produced by the shock must be higher.

In each set of data at a constant Mach number, it was noted that the centerline pressure distribution corresponding to the lowest injection pressure seemed to be somewhat smeared out compared to the others. The pressure changes were more gradual, but extended over a larger region, again in the normalized coordinates. Although no detailed boundary layer studies have yet been made to confirm this supposition, the schlieren and shadowgraph pictures seem to support the notion that this smearing out of the pressure distribution occurs when the scale of the obstruction is of the same order as a characteristic boundary layer thickness. Since the scaling procedure is based upon a single scaling parameter for the flow field, it seems logical that this simplicity would be modified in a region where the scale factor was of the same order as another important characteristic dimension of the flow.

The correlation of the CIT data in Figure 10 is not as good as that of the JPL data presented in Figures 12 through 16, which appears to be excellent. At least some of the scatter in the CIT results is due to the rather crude pressure instrumentation, see page 2. The data for one of the higher pressure-ratio runs of the CIT data with a laminar boundary layer exhibits what appears to be the pressure plateau characteristic of laminar separation. This pressure plateau does not show up clearly in all of the CIT laminar boundary-layer data, as can be seen in Figure 10. It is not known whether this is entirely due to inaccuracies in measurement, or whether the much more pronounced effects of laminar separation exhibited in Figure 14 are primarily a result of actual differences in the shock - boundary layer interaction between the two sets of experiments. In any event, the character of the boundary layer on the tunnel wall in the CIT tunnel would be expected to be different from that in the flat-plate experiments in the JPL tunnel.

Several papers have appeared in the literature which present pressure distributions on flat plates with secondary injection, which are similar to the experiments described in this paper^(2, 6, 7, 8). Data from the paper by Cubbison, Anderson, and Ward⁽⁶⁾ was considered to be the most directly comparable to that which has been presented here. Figure 17 presents six pressure distributions in the plane $y = 0$ for two Mach numbers; the data are plotted in the manner of Figures 10 to 16, except that the original pressure coefficient notation was retained. The agreement is seen to be quite good, except in the separation region upstream of the injector at free-stream Mach number 4.84. It should be noted that for the two largest values of h , at $M_{\infty} = 4.84$, the boundary layer was separated up to the leading edge of the plate, thus precluding any

similarity in that region.

Discussion and Conclusions

Quantitatively, the results of the shock shape, concentration, and pressure measurements indicate that the scaling parameter, h , is satisfactory for the range of variables which has been investigated, with the previously mentioned restriction that the penetration height be large with respect to the separated boundary-layer thickness. The correlation of the shock and concentration data was excellent. Some lack of similarity in the pressure data was observed, primarily in the laminar boundary layer separation region, and at the lower Mach numbers in the reattachment region downstream of the injector. It is also apparent that a simple one-parameter scale transformation cannot give a detailed correlation of the pressure data in these regions.

Review of Flow Models. A number of models have been suggested by other authors which lead to a calculation of a scale height for secondary injection. For example, see References 10 to 13. Unfortunately, most of these models are for two-dimensional flow and are not directly applicable. However, it is still possible to compare their approach to the one used in this paper.

One assumption used was that the penetration height is fixed by the area required to pass the mass flow of injectant after it expands isentropically to the local ambient pressure.⁽¹⁰⁾ In our case, this assumption leads to the result that the penetration height depends only on the ambient static pressure and injectant specific heat ratio, and is independent of the momentum of the free stream. These conclusions are not in agreement with the experimental results. A second type of model, e.g. Reference

11, is based on the assumption that the separated boundary layer is tangent to the top of the injectant stream, and that side force is only generated upstream of the injector port. Our experimental work shows that such a violent separation can only occur when penetration height and boundary layer thickness are of comparable scale. This range of penetration heights was not examined in the present paper.

Furthermore, analysis of the results of Newton and Spaid⁽¹⁴⁾ shows that with gaseous injection, the major portion of the side force is applied downstream of the injector port. They found that there was still a small positive contribution to the side force for $(x/h) > 12$. Although this work was carried out in a conical rocket nozzle, the results should apply at least qualitatively to the present discussion.

Additional information is furnished by analysis of the results of Walker, et al⁽¹⁵⁾, who worked with a conical nozzle which had injector ports of various diameters located close to the nozzle exit. Their values of specific impulse of side injection, I_s , are given in Figure 18 as a function of the ratio of distance between injector port and nozzle exit to values of penetration heights calculated from equation (6). In these experiments, the ratio of the distance between injector and nozzle exit and the penetration height varied from about 2.9 to 8.5, and the corresponding specific impulse for secondary injection increased by a factor of about 1.4. These results can also be interpreted as showing the effect of systematically increasing the wall area on which the pressure disturbances act from an area corresponding to $(X/h) = 2.9$ to $(X/h) = 8.5$. For this configuration the contribution to side force is small when $(X/h) > 7$. This result agrees with the analyses of the data of Newton and Spaid,⁽¹⁴⁾

discussed in the previous paragraph, and shows that the downstream contribution to side force is very important.

A third type of model is that which was proposed by Broadwell.⁽¹²⁾ In this paper, the blast-wave theory was used to obtain a pressure field on a flat plate. The scale of this pressure field was determined by calculating a value for drag produced by injection and equating this to the energy added to the free stream per unit length. This drag is therefore completely analogous to the change in the x-component of momentum of the jet in the present model, equations (3), (4), and (5). A value of drag, then, corresponds to a scale height, so that these two approaches can be compared. In Reference 12, the drag, or energy per unit length, is calculated by assuming first, that the injected material reaches the velocity of the undisturbed free stream, and second, that the effect of adding mass can be taken into account by adding heat to a part of the free-stream flow sufficient to produce the same volume change which would be produced by mass addition. The result of this calculation is as follows:

$$D = \dot{m}_j V_\infty \left[1 + \frac{2 + (\gamma_\infty - 1) M_\infty^2}{2(\gamma_\infty - 1) M_\infty^2} \frac{\dot{m}_\infty}{\dot{m}_j} \frac{T_{oj}}{T_{o\infty}} \right] \quad (10)$$

In order to compare the effect of these assumptions with the present model, an equation for scale height similar to equation (6) was derived by substituting equation (10) for equation (5) in the present derivation. The resulting equation, analogous to equation (6), gave very nearly the same Mach number dependence as equation (6), but showed a strong dependence upon the molecular weight of the injectant at a constant value of free stream - to - injection pressure ratio. This dependence was not observed. These results indicate that the scale of the flow field is probably determined by an isentropic expansion of the jet in the immediate vicinity

of the injector, rather than by the acceleration and mixing process between the jet and the free-stream material which occurs farther downstream. These results and conclusions are also in accord with the fact that the drag of a slender, blunt-nosed body at high Mach numbers is determined almost entirely by the characteristic nose bluntness dimension.⁽³⁾

Review of the Flow Field Characteristics. The concentration and pressure data have now made it possible to add some details to the qualitative description of the flow field which was presented earlier. It has been shown that the jet mixes very rapidly as it leaves the injector, and much more slowly for (x/h) greater than about 4. The jet is approximately parallel to the wall at $(x/h) \approx 3$.

A pair of vortices appear to be shed from the jet near the injector; these accelerate the mixing process and result in a region of low concentration of injectant material in a region immediately downstream of the jet near the wall. The flow appears to reattach to the wall in the region $3 \lesssim (x/h) \lesssim 4$. This reattachment may be accompanied by a compression wave system, increasing in strength with jet-to-free stream stagnation pressure ratio and with decreasing free-stream Mach number.

The character of the boundary layer separation for the case of injection into a turbulent boundary layer is quite different from the separation of a laminar boundary layer. The pressure rise due to turbulent separation extends only slightly upstream of the bow shock, but the laminar boundary layer separates far upstream. In neither case, however, does the height of the separated boundary layer approach the height of the jet, if the jet height is much greater than the undisturbed boundary layer thickness. This result is quite different from the results obtained in boundary-layer separation studies with a two-dimensional step.⁽⁹⁾ Part

of this difference seems to be the result of the inherent difference between two- and three-dimensional obstructions; the boundary layer can simply go around the three-dimensional object, but the flow must all go over the top of the two-dimensional one. In addition, there is the previously mentioned effect of the jet shape near the wall which tends to provide clearance for the boundary layer.

Scaling Laws for Side Force on a Wall. If the scaling law, as developed earlier in equation (6), can be taken as being a good approximation, then it is easy to predict the variation of the side force generated on an infinite flat surface by the variation of the jet parameters. For many purposes, it is desirable to know the change in force produced on the wall by secondary injection.

The side force contribution from the pressure field resulting from secondary injection from an infinite flat plate can be expressed as:

$$\Delta F = \int_{x=-\infty}^{\infty} \int_{y=-\infty}^{\infty} (P - P_{\infty}) dx dy . \quad (11)$$

Dividing through by $(P_{\infty} h^2)$ we have:

$$\frac{\Delta F}{P_{\infty} h^2} = \int_{\frac{x}{h}=-\infty}^{\infty} \int_{\frac{y}{h}=-\infty}^{\infty} \frac{P - P_{\infty}}{P_{\infty}} \frac{dx}{h} \frac{dy}{h} = \Phi . \quad (12)$$

The integral of equation (12) is evaluated in the normalized coordinates, and therefore will depend only upon the free-stream Mach number and specific heat ratio. That is,

$$\Phi = \Phi \{M_{\infty}, \gamma_{\infty}\} .$$

The total side force due to injection F_s is the sum of the interaction force, ΔF , and the thrust of the injectant, F_j . The thrust of a sonic jet is given by

$$F_j = P_{o_j} A_j C_f \{M=1\} \quad (13)$$

where

$$C_f \{M=1\} = \left(\frac{2 \gamma_j}{\gamma_j + 1} \right)^{\frac{1}{\gamma_j - 1}} - \frac{P_\infty}{P_{o_j}} \quad (14)$$

Combining (6), (12), (13), (14), we have

$$\frac{\Delta F}{F_j} = \frac{8 \Phi \gamma_j}{\pi M_\infty^2 C_p^* \gamma_\infty} \frac{\left\{ \left[\frac{2}{\gamma_j - 1} \left(\frac{2}{\gamma_j + 1} \right)^{\frac{\gamma_j + 1}{\gamma_j - 1}} \right] \left[1 - \left(\frac{P_\infty}{P_{o_j}} \right)^{\frac{\gamma_j - 1}{\gamma_j}} \right] \right\}^{\frac{1}{2}}}{\left[\left(\frac{2 \gamma_j}{\gamma_j + 1} \right)^{\frac{1}{\gamma_j - 1}} - \frac{P_\infty}{P_{o_j}} \right]} \quad (15)$$

If we define

$$\Gamma = \frac{\left[1 - \left(\frac{P_\infty}{P_{o_j}} \right)^{\frac{\gamma_j - 1}{\gamma_j}} \right]^{\frac{1}{2}}}{1 - \left[\left(\frac{\gamma_j + 1}{2 \gamma_j} \right)^{\frac{1}{\gamma_j - 1}} \right] \frac{P_\infty}{P_{o_j}}} \quad (16)$$

then (15) becomes

$$\frac{\Delta F}{F_j} = \frac{8 \Phi \Gamma}{\pi M_\infty^2 C_p^* \gamma_\infty \sqrt{1 - (1/\gamma_j^2)}} \quad (17)$$

Γ is a slowly varying function of γ_j and P_∞/P_{o_j} for the range of these variables which is of interest. For the special case that $P_\infty \ll P_{o_j}$, it is evident that the interaction force is directly proportional to the jet thrust.

The usual form for presentation of rocket motor tests has been to

give the ratio of side force to axial force as a function of the ratio of secondary to primary mass flow rates. That is,

$$F_s/F_p = f(m_j/m_p).$$

Results from (17) can be compared with rocket motor data in the following way:

$$F_s = F_j + \Delta F$$

$$F_s = F_j \left[1 + \frac{8\Phi\Gamma\left(\gamma_j, \frac{P_\infty}{P_{o_j}}\right)}{\pi M_\infty^2 C_p^* \gamma_\infty \sqrt{1 - (1/\gamma_j^2)}} \right] \quad (18)$$

where the thrust of a sonic jet written in terms of m_j is

$$F_j = m_j \sqrt{\frac{2R_j T_{o_j}}{\gamma_j(\gamma_j+1)}} \left[\gamma_j + 1 - \left(\frac{\gamma_j+1}{2} \right)^{\frac{\gamma_j}{\gamma_j-1}} \frac{P_\infty}{P_{o_j}} \right]. \quad (19)$$

Equations (18) and (19) can be used to correlate side force measurements if the dimensionless pressure integral, Φ , is known.

Even when Φ is not known, correlation can be made if the factors directly multiplying Φ in equation (18) are held fixed. This condition implies that valid comparisons can be made when any of the following parameters are changed: injectant molecular weight and total temperature; injector diameter; and primary-stream molecular weight and total temperature. In addition, the dependence of Γ and the square bracketed term in equation (19) on P_{o_j} is very weak. Hence, a change in the ratio (P_{o_j}/P_∞) will only introduce a slight error in scaling.

Subject to the above restrictions, it is evident that

$$F_s \propto m_j \sqrt{R_j T_{o_j}}.$$

In addition, if changes in axial thrust of the primary flow caused by non-optimum expansion and by secondary injection are neglected, then

$$F_p \propto \dot{m}_p \sqrt{R_p T_{o_p}}$$

and therefore

$$\left(\frac{F_s}{F_p} \right) \propto \frac{\dot{m}_j}{\dot{m}_p} \sqrt{\frac{R_j T_{o_j}}{R_p T_{o_p}}} = \frac{\dot{m}_j}{\dot{m}_p} \sqrt{\frac{T_{o_j}/m_j}{T_{o_p}/m_j}} \quad (20)$$

This result indicates that the thrust ratio depends directly on the mass flow rate and on the square root of the ratio of injectant total temperature to molecular weight. The ratio is independent of injector diameter.

The discussion given in the earlier sections of this paper indicates that there are a number of restrictions which must be placed on this scaling procedure. Clearly, the procedure is strictly applicable only if the wall on which the pressure disturbances exist is of sufficient extent that the pressure at its boundaries has returned to the free-stream static pressure. In practice, this means that the boundaries must be at least 10h away from the injector.

In addition to this geometric limitation, it will be useful to summarize again the limitations on the scaling procedure itself. First, it is necessary that the penetration height be larger than the separated boundary layer thickness.

Second, if the boundary layer is turbulent, scaling appears to be excellent except in the reattachment region. If scaling of a nozzle is carried out by using geometrically similar devices with equal total pressure ratios, (P_{o_j}/P_{o_∞}) , then the reattachment phenomena will also be similar and no scaling errors will be introduced. This scaling procedure is that which is most likely to be used in the design of a large rocket

nozzle where the boundary layer is almost certainly turbulent.

Third, if the boundary layer is laminar, upstream separation phenomena are more important, and scaling with the penetration height may be less satisfactory. In this case, there is some indication that pressure changes compensate each other,⁽¹³⁾ however, no information on such compensation can be deduced from the present work.

Some direct comparison can be made of the scaling law developed here with experimental rocket engine tests. Even though the flow field in a nozzle is not directly comparable to that treated here, it is felt that the general conclusions drawn from the present work are useful.

Rodriguez⁽¹⁶⁾ and many other experimenters have found that the side force is independent of the injector port area for fixed mass flow and depends linearly on the mass flow of injectant when the primary flow parameters are held fixed. This result agrees with that obtained from equation (15).

Some work has been carried out in which injectants with different total temperatures and different molecular weights were used.^(15,17,18) The correlation proposed by Lingen⁽¹⁷⁾ and later approximately verified by Chamay and Sederquist⁽¹⁸⁾ agrees exactly with equation (20).

Figure 19 shows data from Reference 17 for gas injection into a rocket nozzle. The parameter (T_{o_j} / T_{o_p}) was changed by a factor of more than 6 for the two cases, and the agreement is excellent, although the data are badly scattered. Figure 20 shows data for nitrogen and hydrogen injection into a rocket nozzle, from Reference 18. The scatter here is much smaller than for Figure 17, but the correlation is not quite so good. It can be seen that the correlation improves with increasing m_j , so that there is about 10 per cent difference between the

nitrogen and hydrogen data at the higher injection rates.

In the previously mentioned paper by Walker, et al., data are reported for injection of different gases into a rocket nozzle. The correlation of these data by the present treatment is presented in Figure 21a. Only data for sonic injection are presented. The choice of h^2 as a correlating parameter was made because it accounts for variations in γ_j and P_∞/P_{o_j} . It can be seen that the effect of injector diameter is accounted for quite well, but considerable systematic variation remains among data for different gases. It is interesting to note that the correlation is in error by about the same factor over the entire range of h^2 , or injection rate, in contrast to the data of Reference 18.

The different treatment proposed by Broadwell⁽¹⁹⁾ gives a somewhat better correlation of the data of Reference 15, particularly at the higher injection rates (see Figure 21b). Figure 21b also includes data for subsonic injection, but does not include the effect of injector port diameter. In another figure of Reference 19, Broadwell shows a correlation of this effect which is as good as that in Figure 21a.

Because of the disagreement between the various sets of experimental data of References 15, 17, and 18, it is difficult to judge the value of the present technique in correlating rocket motor data for different gaseous injectants. Both the technique proposed by Broadwell and that proposed by the authors appear to be in approximate agreement with experimental data, although both techniques predict greater increases in performance with decreasing molecular weight of injectant than are actually realized.

In the case of the technique developed here, the explanation for this discrepancy is believed to be as follows. The assumption of isen-

tropic expansion of the secondary flow appears to be quite satisfactory in the vicinity of the injector. However, it has been demonstrated for gaseous injection into a rocket exhaust that in many configurations, a major portion of the side force is developed quite far downstream of the injector. The concentration measurements which have been presented here show that mixing of the injectant with the free stream is quite rapid, so that the speed of the injected gas downstream of the injector is strongly affected by the free stream flow. The effective scale of the obstruction downstream of the injector will then be less than that predicted by equation (6) if the speed of the injectant corresponding to an isentropic expansion to the free-stream static pressure is significantly greater than the speed of the free stream. This effect of mixing will then result in lower performance for a light gas than for a heavy gas when they are compared at the same value of the scale parameter, h , for rocket-nozzle injection configurations for which the side force contribution downstream of the injector is important.

References

1. J. F. Newton Jr. and M. W. Dowdy: paper to be published at JPL.
2. J. L. Amick and P. B. Hays: "Interaction Effects of Side Jets Issuing from Flat Plates and Cylinders Aligned with a Supersonic Stream," WADD Technical Report 60-329 (June 1960).
3. G. G. Chernyi: Introduction to Hypersonic Flow, R. F. Probstein, ed. Academic Press, New York (1961).
4. L. Lees: "Hypersonic Flow," Proc. 5th Internatl. Aero. Conf., Los Angeles. Inst. Aero. Sci., New York (1955), pp. 241-276.
5. J. F. Keffer and W. D. Baines: "The Round Turbulent Jet in a Cross-Wind," Journal of Fluid Mechanics, Vol. 15, No. 4 (April 1963), pp. 481-496.
6. R. W. Cubbison, B. H. Anderson, and J. J. Ward: "Surface Pressure Distributions with a Sonic Jet Normal to Adjacent Flat Surfaces at Mach 2.92 to 6.4," NASA TN D-580 (February 1961).
7. J. J. Janos: "Loads Induced on a Flat-Plate Wing by an Air Jet Exhausting Perpendicularly Through the Plate and Normal to a Free-Stream Flow of Mach Number 20," NASA TN D-649 (March 1961).
8. W. Lefko: "Loads Induced on a Flat Plate at a Mach Number of 4.5 with a Sonic or Supersonic Jet Exhausting Normal to the Surface," NASA TN D-1935 (July 1963).
9. I. E. Vas and S. M. Bogdonoff: "Interaction of a Turbulent Boundary Layer with a Step at $M = 3.85$," AFOSR TN 55-200 (April 1955).
10. P. W. Vinson, J. L. Amick, and H. P. Liepmann: "Interaction Effects Produced by Jet Exhausting Laterally Near Base of Ogive-Cylinder Model in Supersonic Main Stream," NASA Memo 12-5-58W (February 1959).
11. J. M. Wu, R. L. Chapkis, and A. Mager: "Approximate Analysis of Thrust Vector Control by Fluid Injection," ARS Journal, Vol. 31, No. 12 (December 1961), pp. 1677-1685.
12. J. E. Broadwell: "An Analysis of the Fluid Mechanics of Secondary Injection for Thrust Vector Control (Revised)," Space Technology Laboratories, Inc., Report No. 6120-7744-MU-000 (15 March 1962).
13. C. Ferrari: "Interference Between a Jet Issuing Laterally from a Body and the Enveloping Supersonic Stream," The Johns Hopkins University, Applied Physics Lab., Bumblebee Report No. 286, (April 1959).

14. J. F. Newton, Jr. and F. W. Spaid: "Experiments on the Interaction of Secondary Injectants and Rocket Exhaust for Thrust Vector Control," Jet Propulsion Laboratory Technical Report 32-203 (12 February 1962). (Also ARS Journal, Vol. 32, No. 9 (August 1962), pp. 1203-1211.)
15. R. E. Walker, A. R. Stone, and M. Shandor: "Secondary Gas Injection in a Conical Rocket Nozzle I. Effect of Orifice Diameter and Molecular Weight of Injectant," AIAA Journal, Vol. 1, No. 2 (February 1963), pp. 334-338. (See also Ref. 24 of this paper.)
16. C. J. Rodriguez: "An Experimental Investigation of Jet-Induced Thrust Vector Control Methods," presented at the 17th Annual JANAF-ARPA-NASA Solid Propellant Meeting, Denver, Colorado (23-25 May 1961).
17. A. Lingen: "Jet-Induced Thrust-Vector Control Applied to Nozzles Having Large Expansion Ratios," United Aircraft Corp. Research Dept. Report R-0937-33 (1 March 1957).
18. A. J. Chamay and R. A. Sederquist: "An Experimental Investigation of Shock Vector Control with Gaseous Secondary Injection" ARS Preprint 2216-61 (August 1961).
19. J. E. Broadwell: "Correlation of Rocket Nozzle Gas Injection Data," AIAA Journal, Vol. 1, No. 8 (August 1963), pp. 1911-1913.

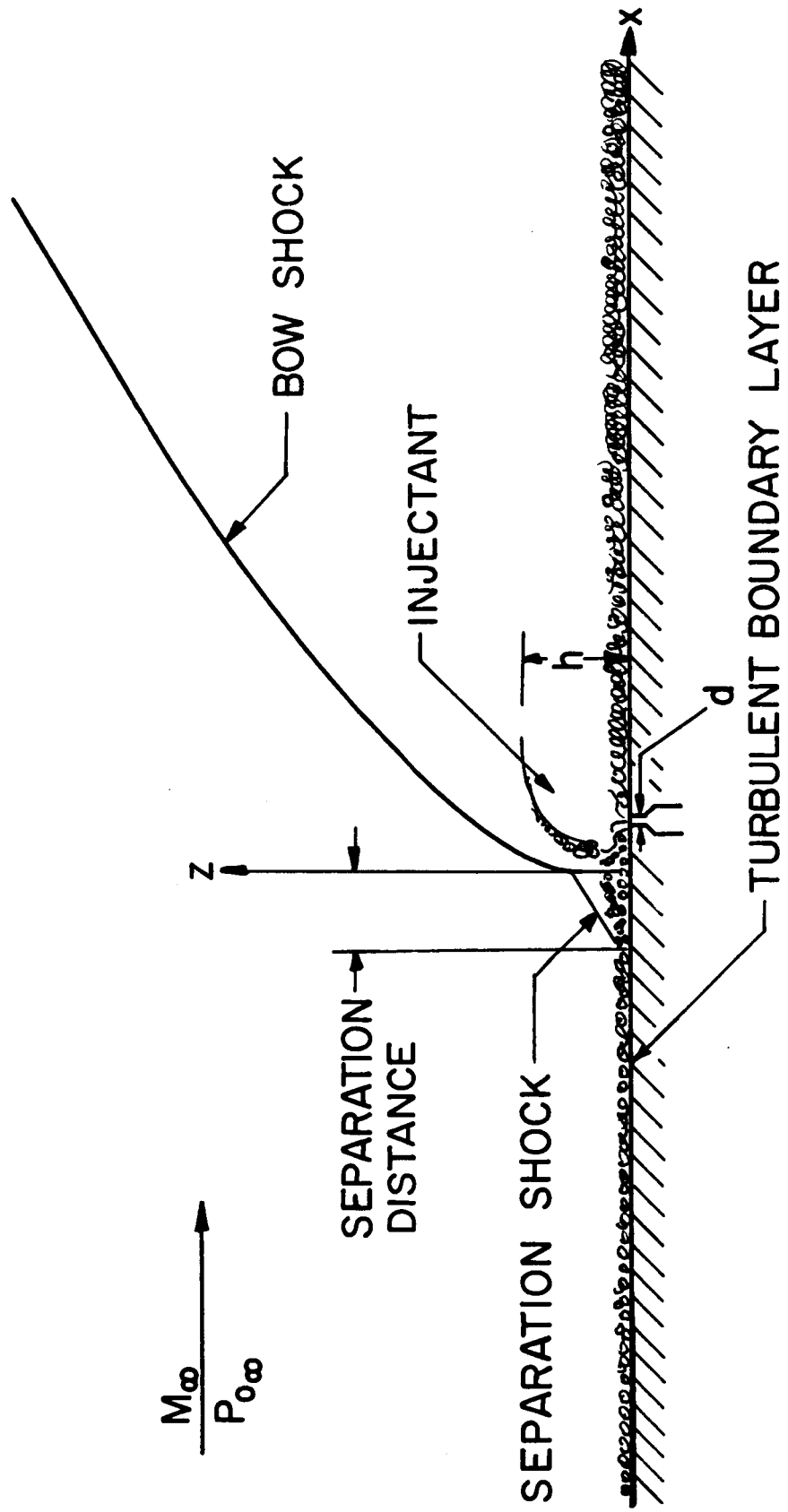


Fig. 1a Sketch of the flow field, turbulent boundary layer.

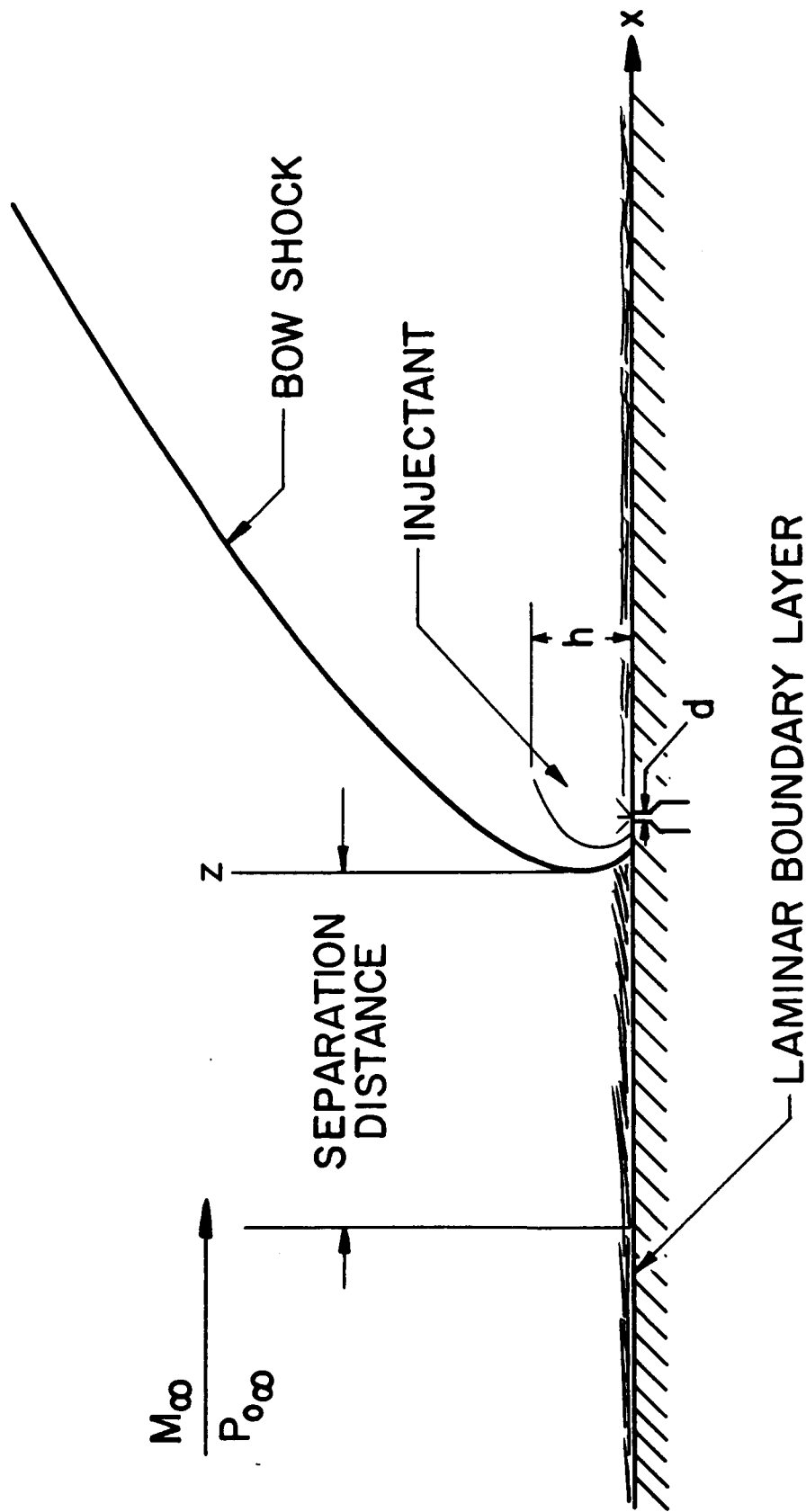


Fig. 1b Sketch of the flow field, laminar boundary layer.

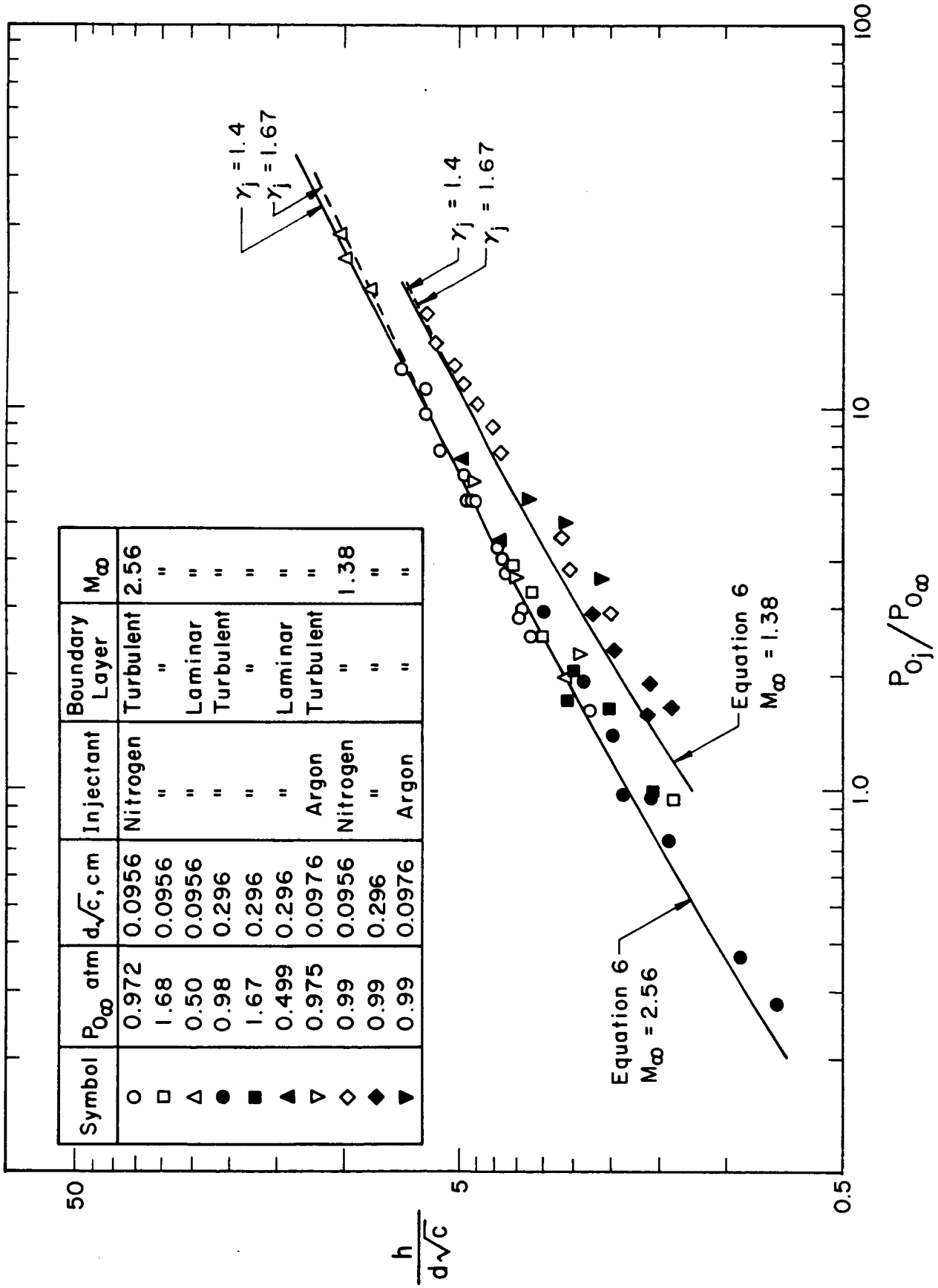


Fig.2 Penetration of secondary jet into primary flow, nozzle wall data.

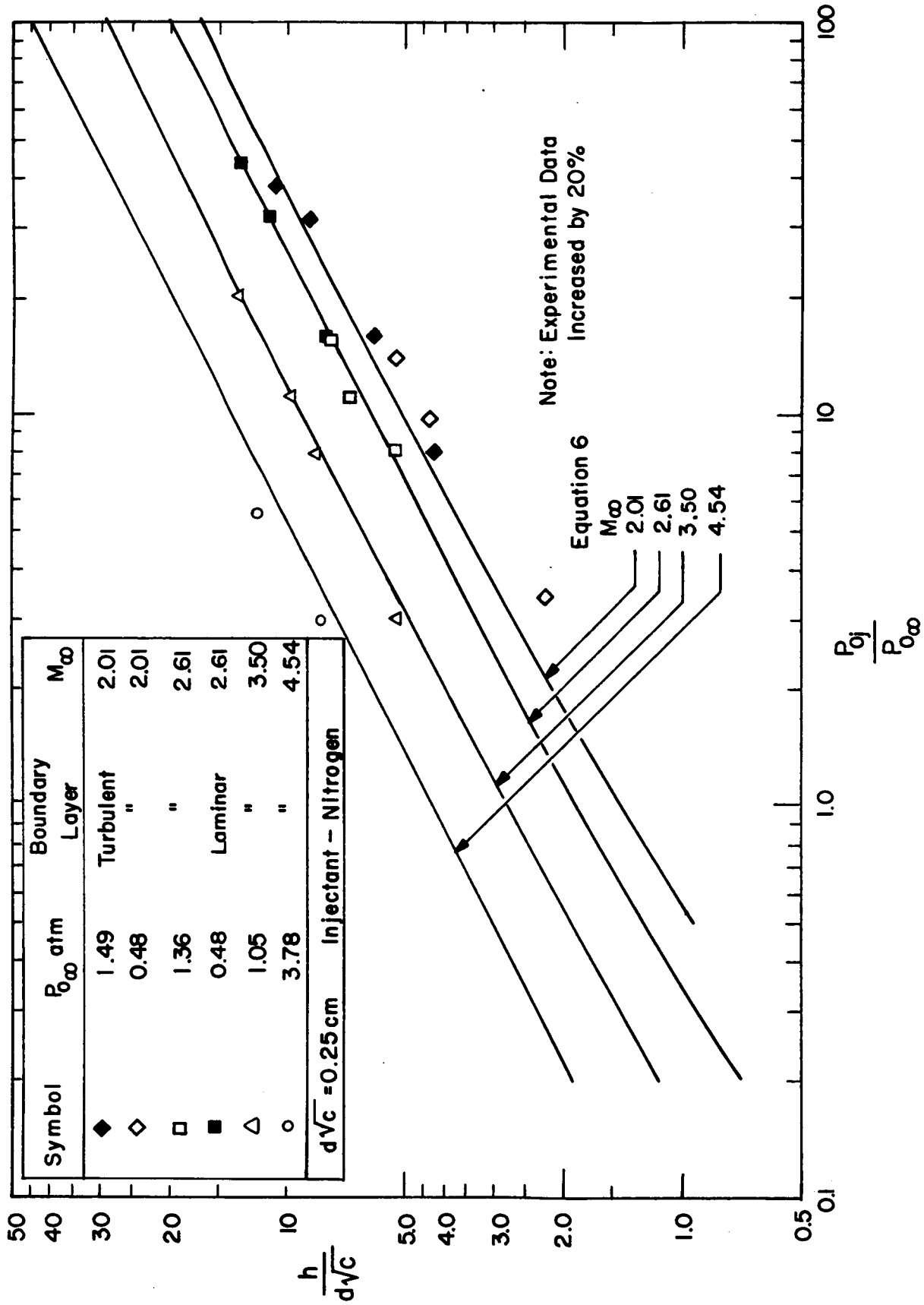


Fig. 3 Penetration of secondary jet into primary flow, flat plate data.

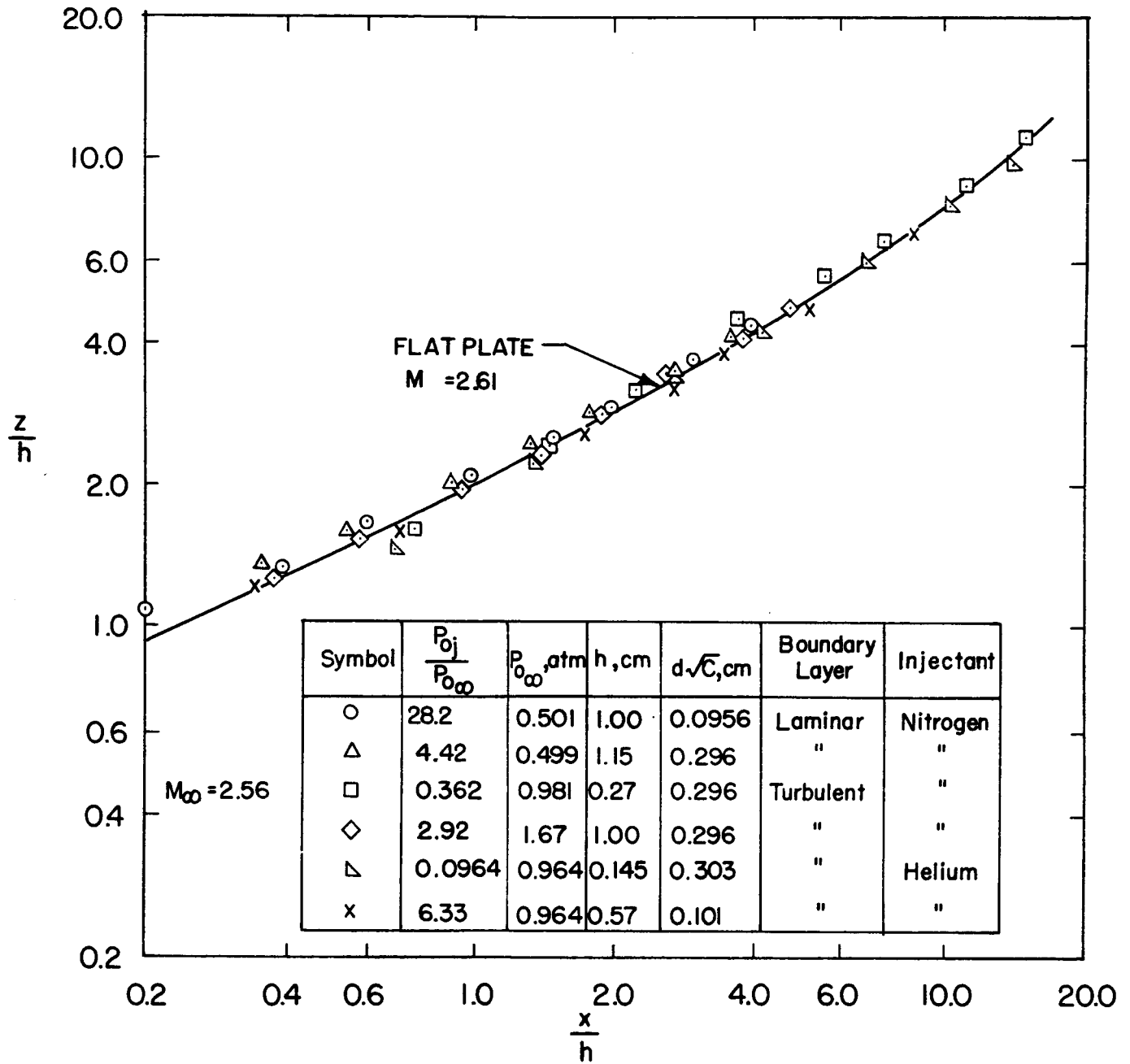


Fig. 4 Shock shapes, comparison of nozzle wall and flat plate results.

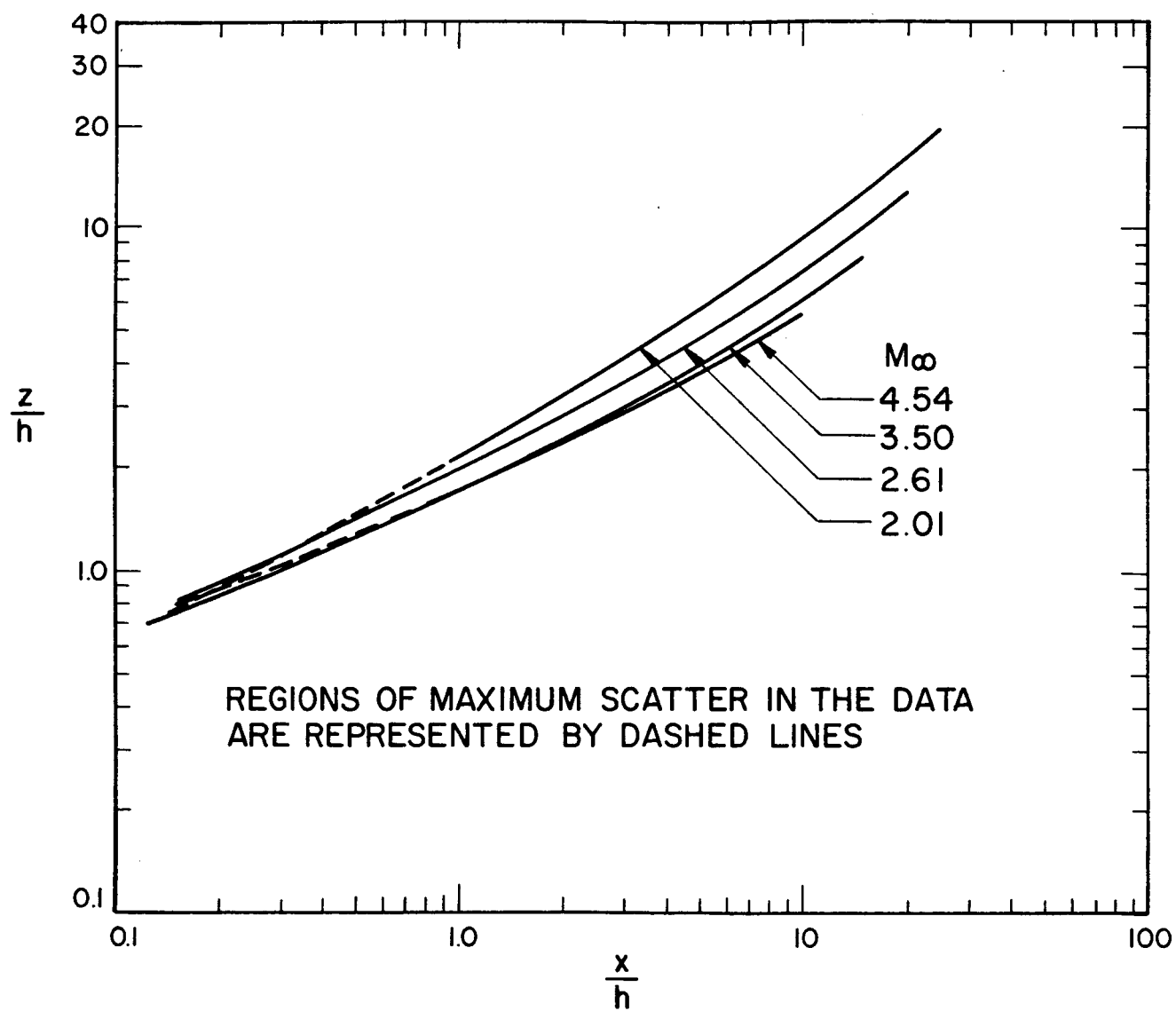


Fig. 5 Shock shapes showing Mach number effect.

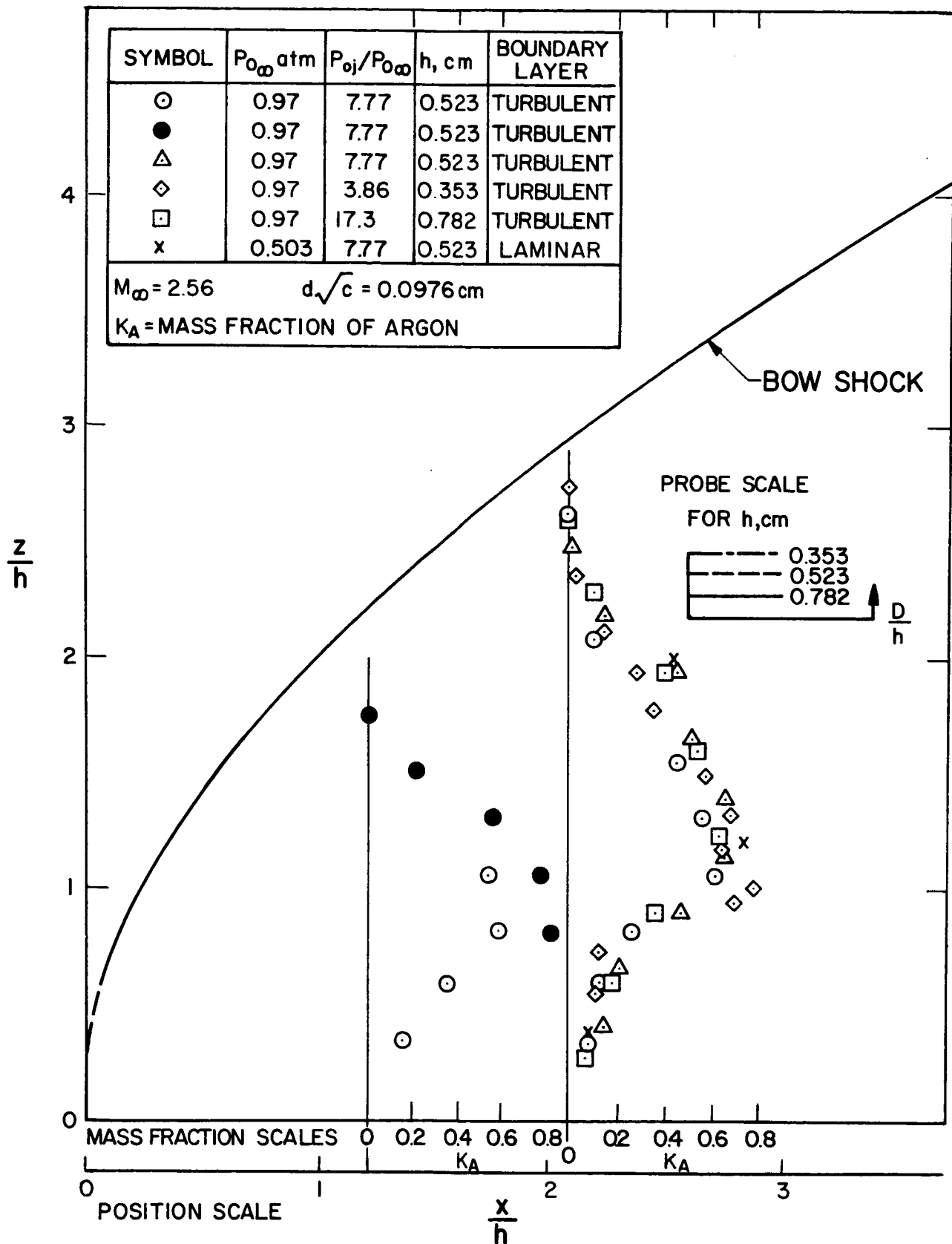


Fig. 6a Concentration measurements with argon injection in the plane $(y/h)=0$, downstream region.

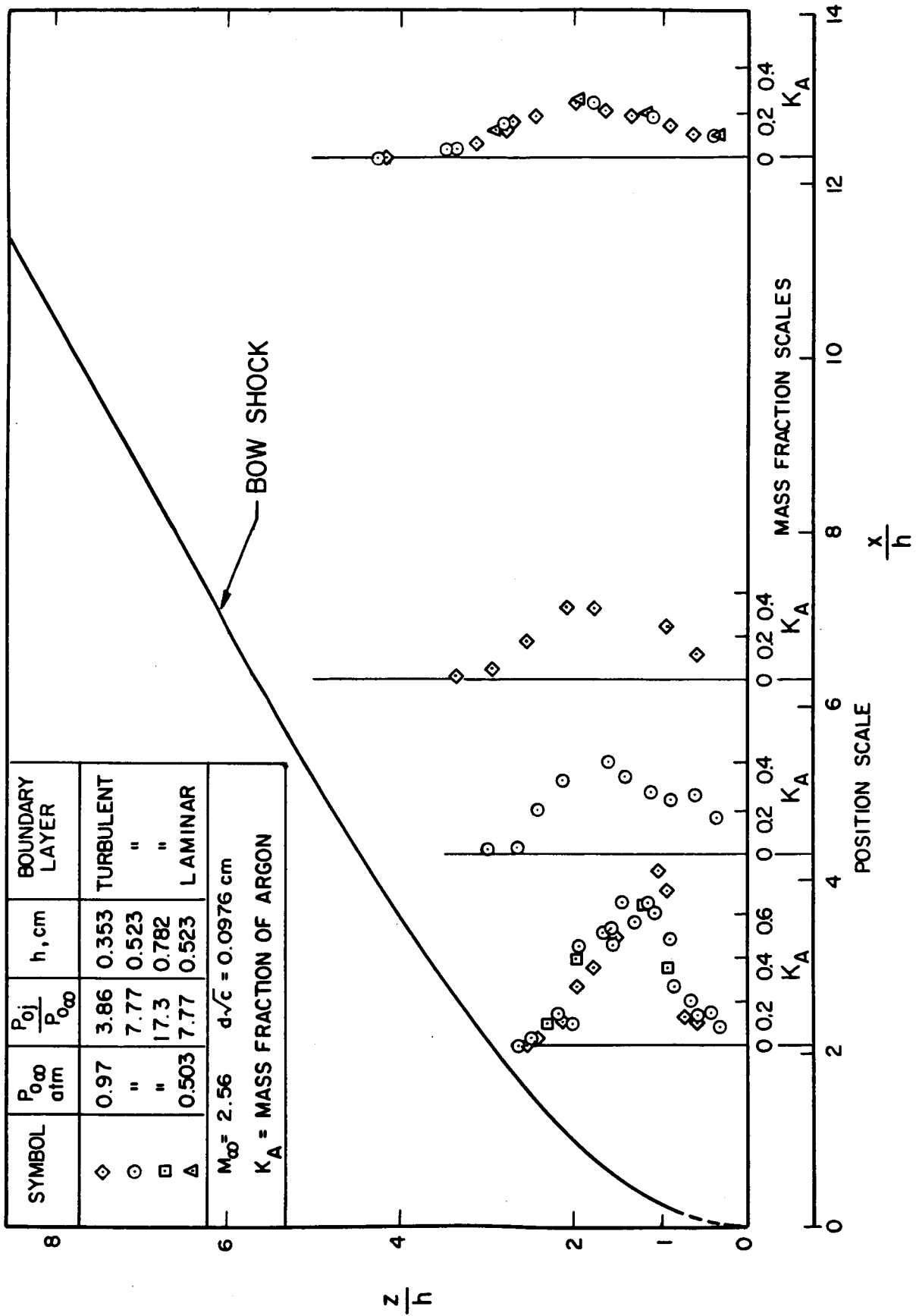


Fig. 6b Concentration measurements with argon injection in the plane $(y/h) = 0$, downstream region.

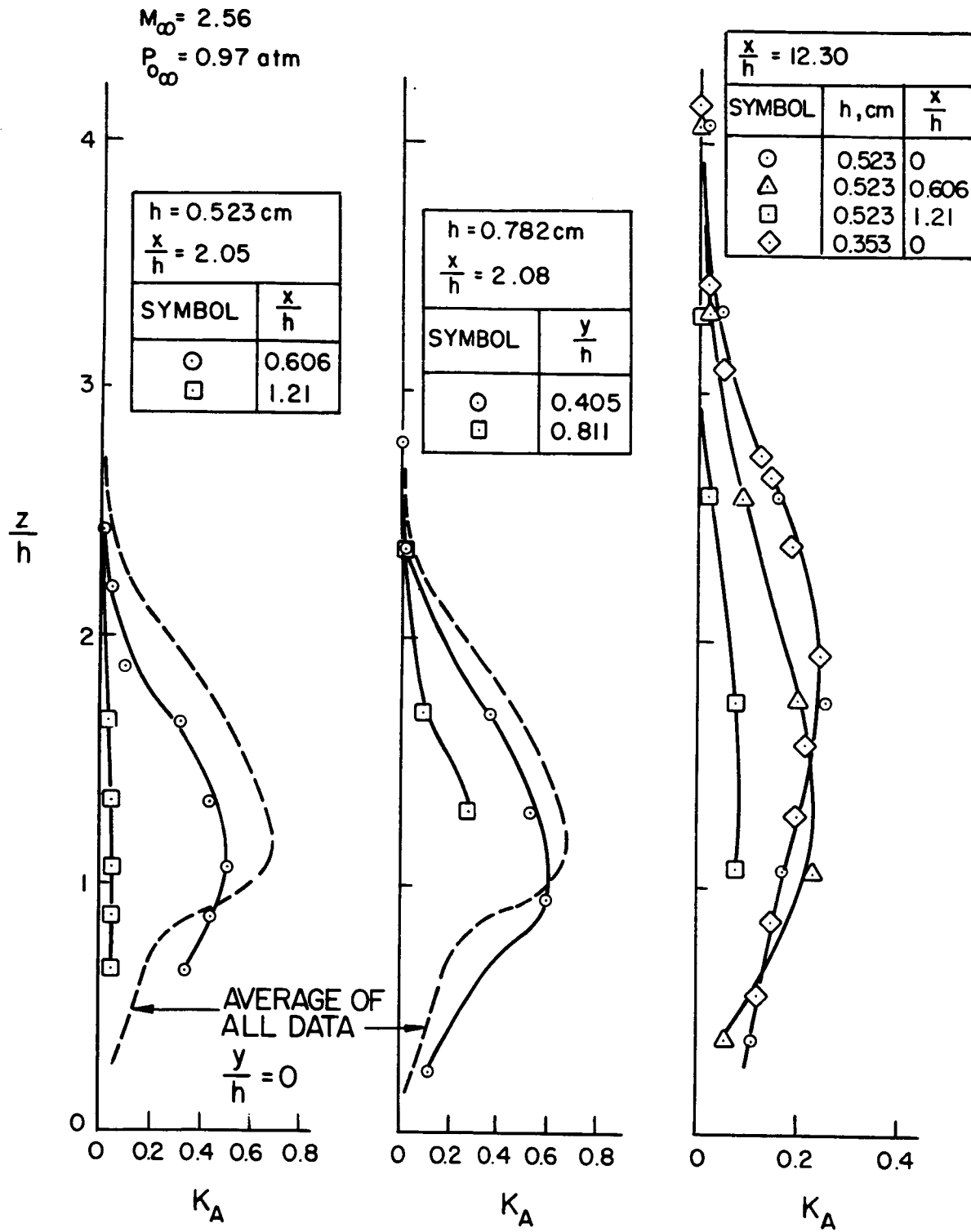


Fig. 7 Concentration profiles in several planes,
 $(y/h) = \text{constant}$.

$M\omega = 2.56$
 $P_{0\omega} = 0.97 \text{ atm}$

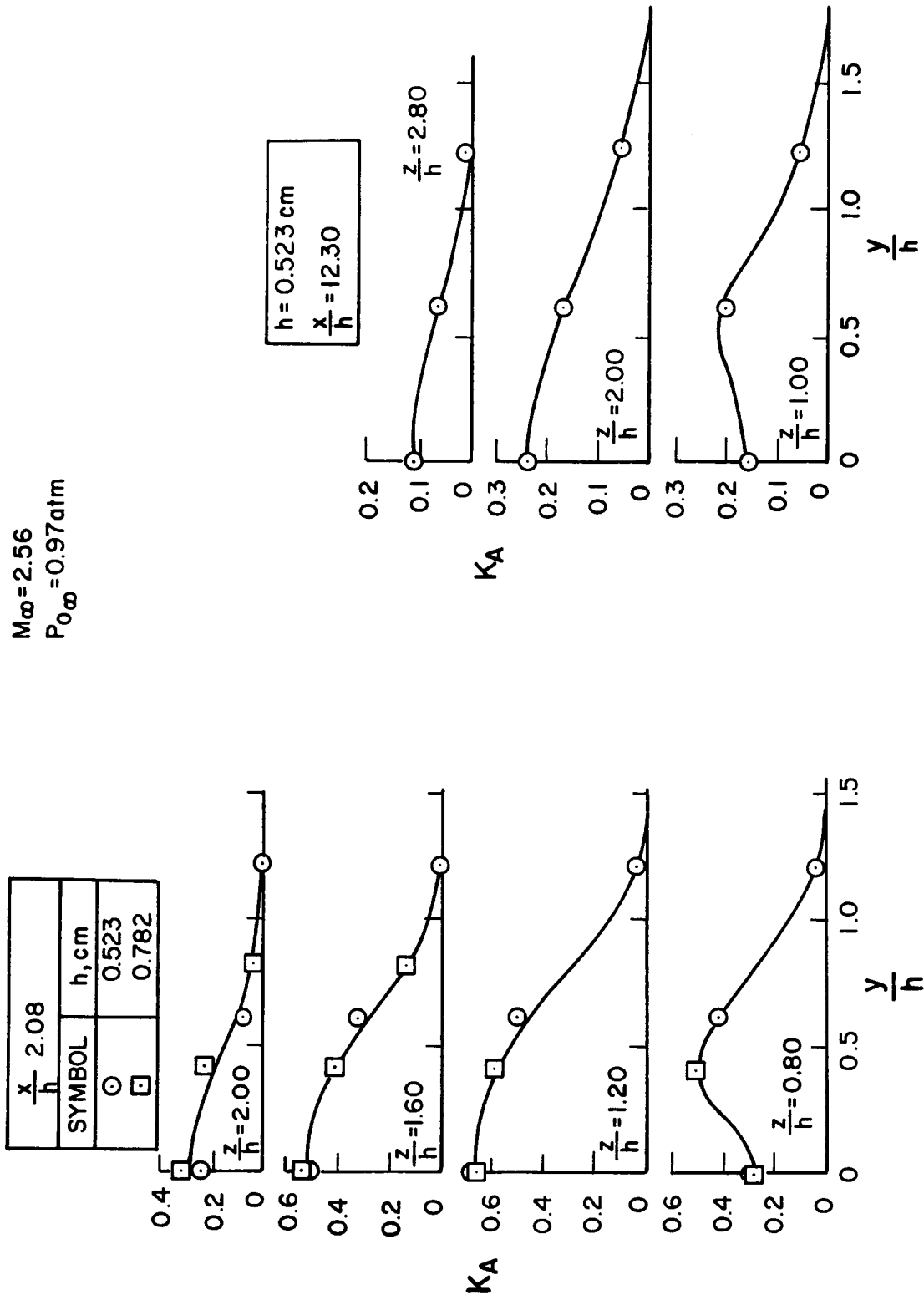


Fig. 8a Crossplots of argon concentration profiles in planes for which $(z/h) = \text{constant}$.

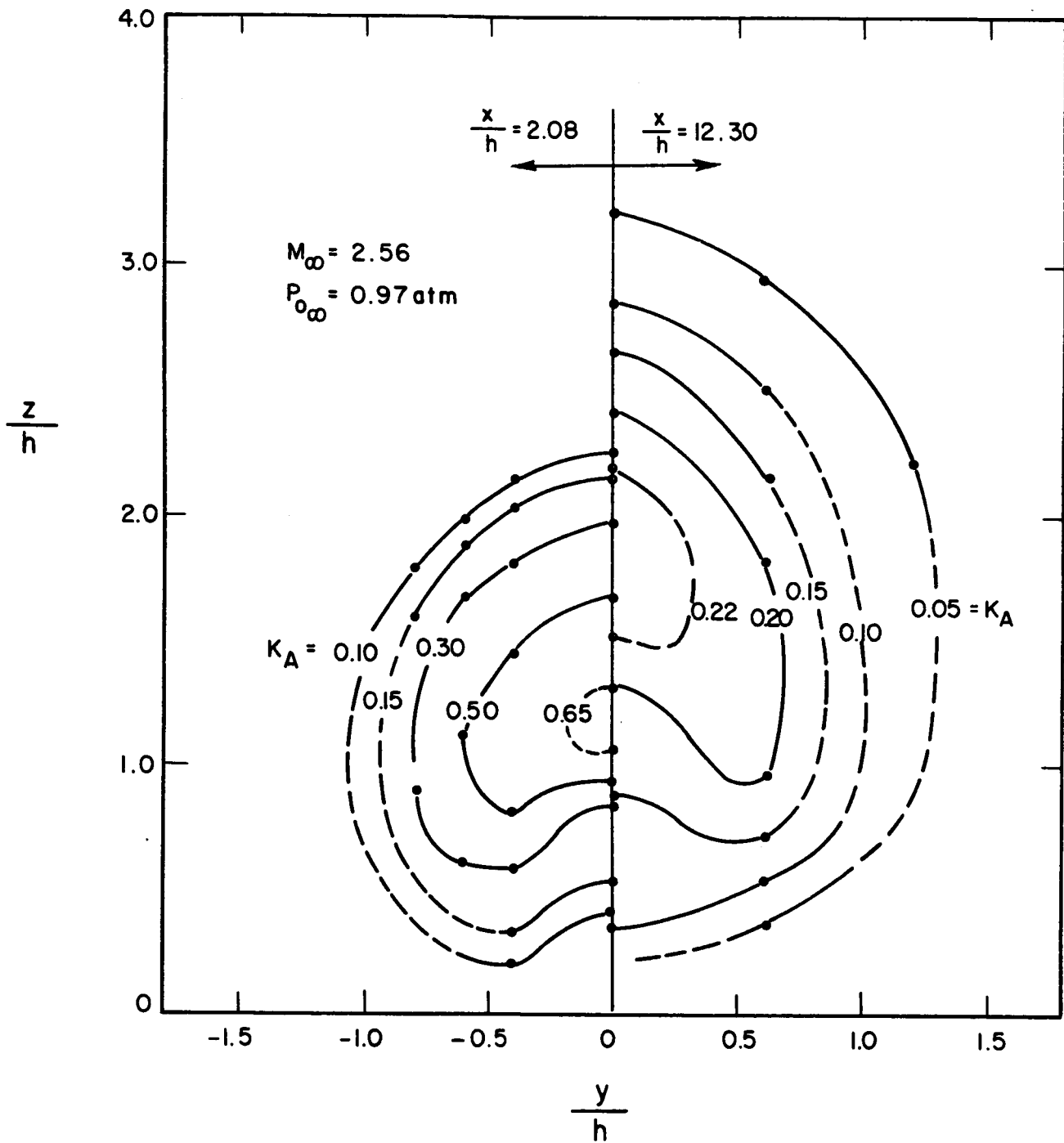
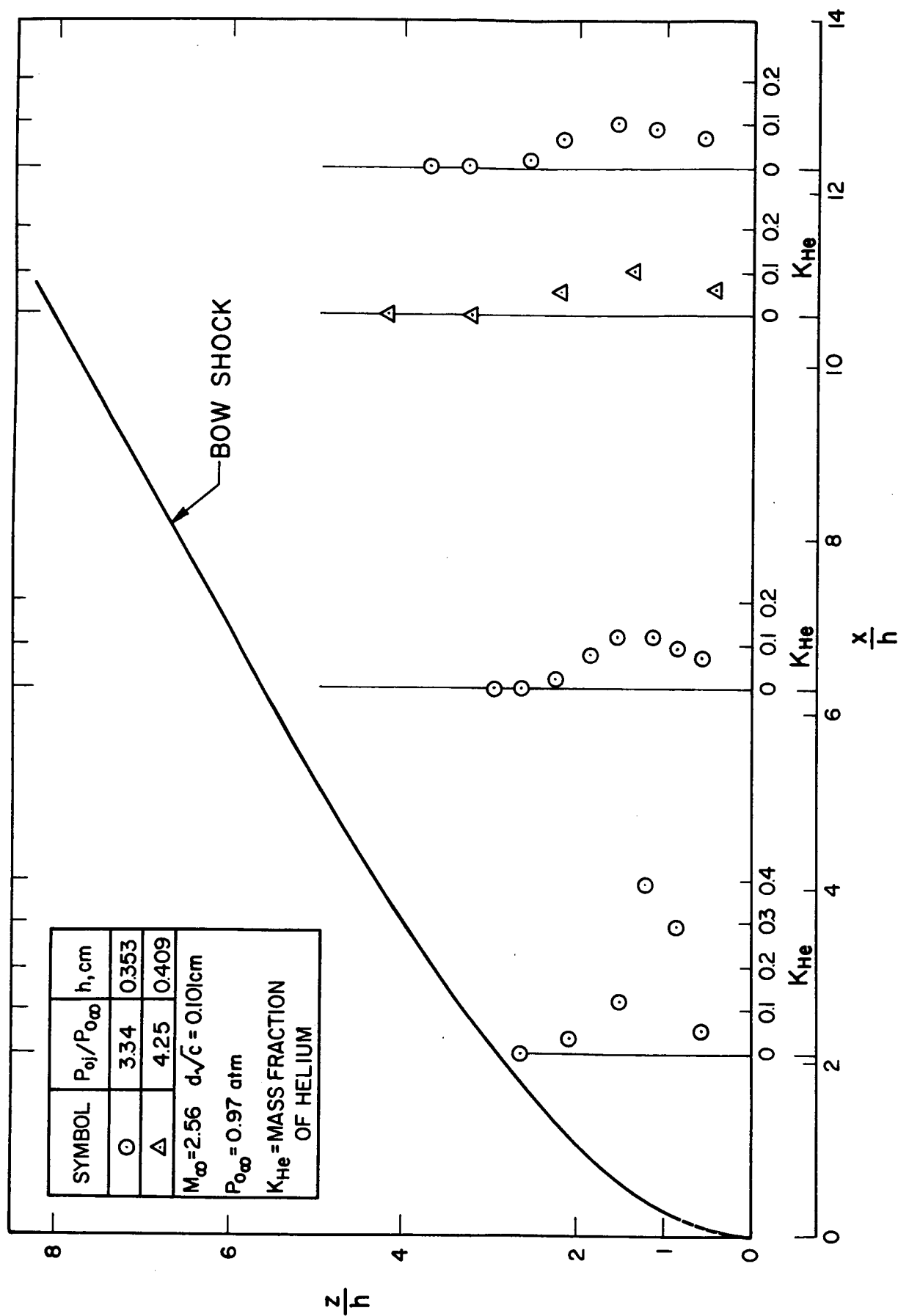


Fig. 8b Concentration contours in the planes $(x/h) = 2.08$ and $(x/h) = 12.30$.

Fig. 9a Concentration measurements with helium injection in the plane $(y/h) = 0$.

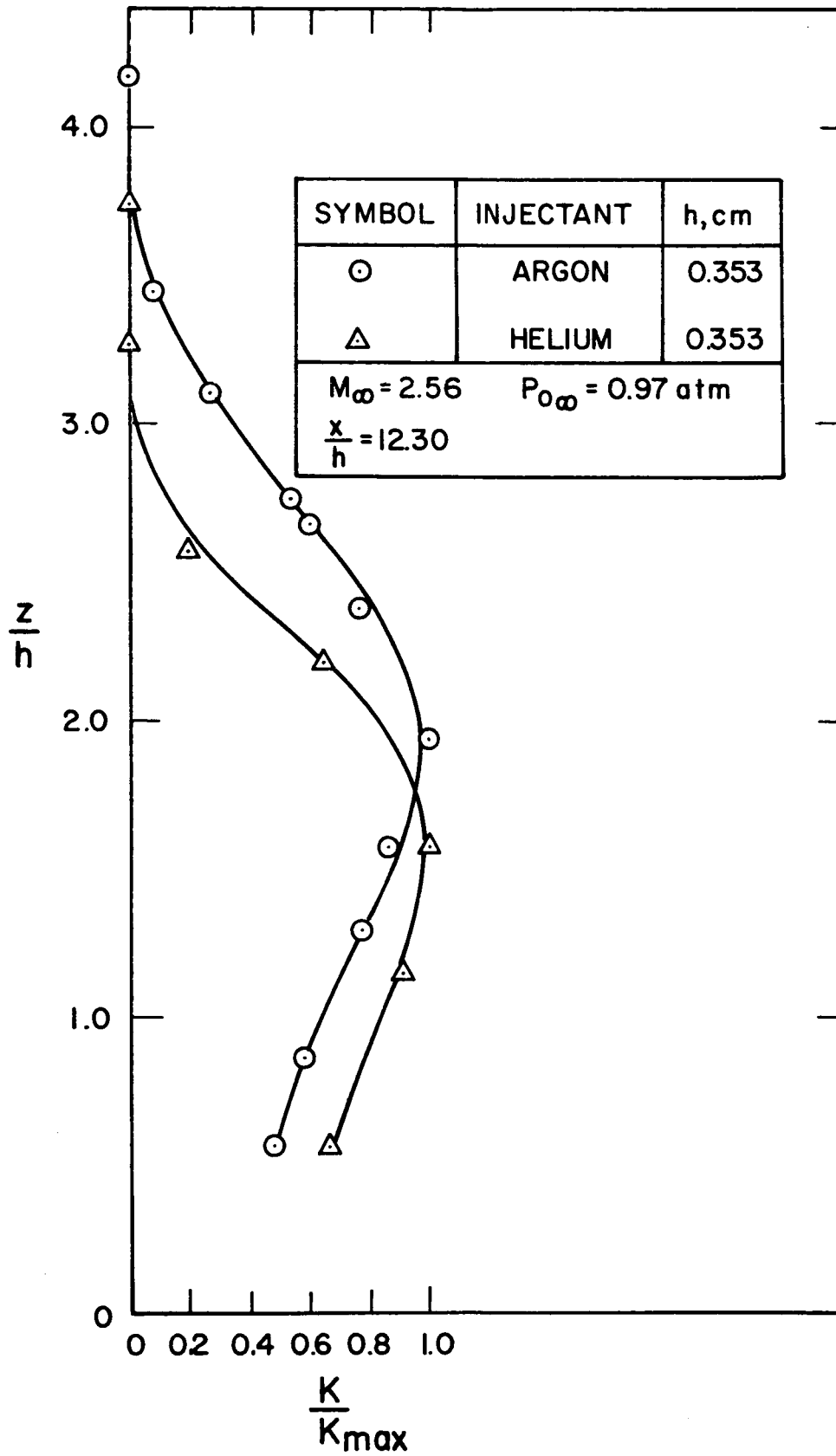


Fig. 9b Comparison of argon and helium concentration data.

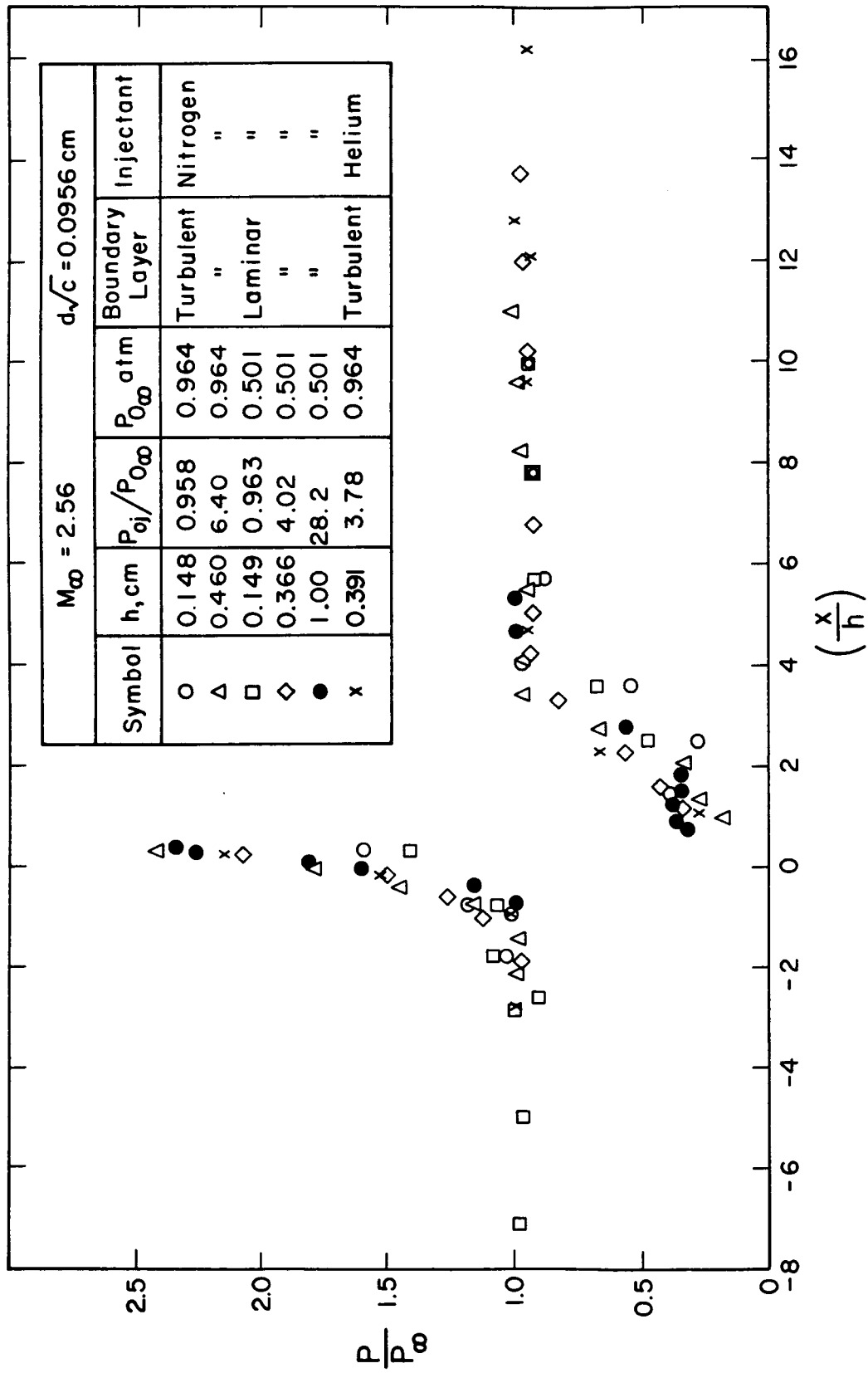


Fig.10 Nozzle-wall static pressure measurements in the $(y/h)=0$ at $M_\infty = 2.56$, with nitrogen and helium injectants.

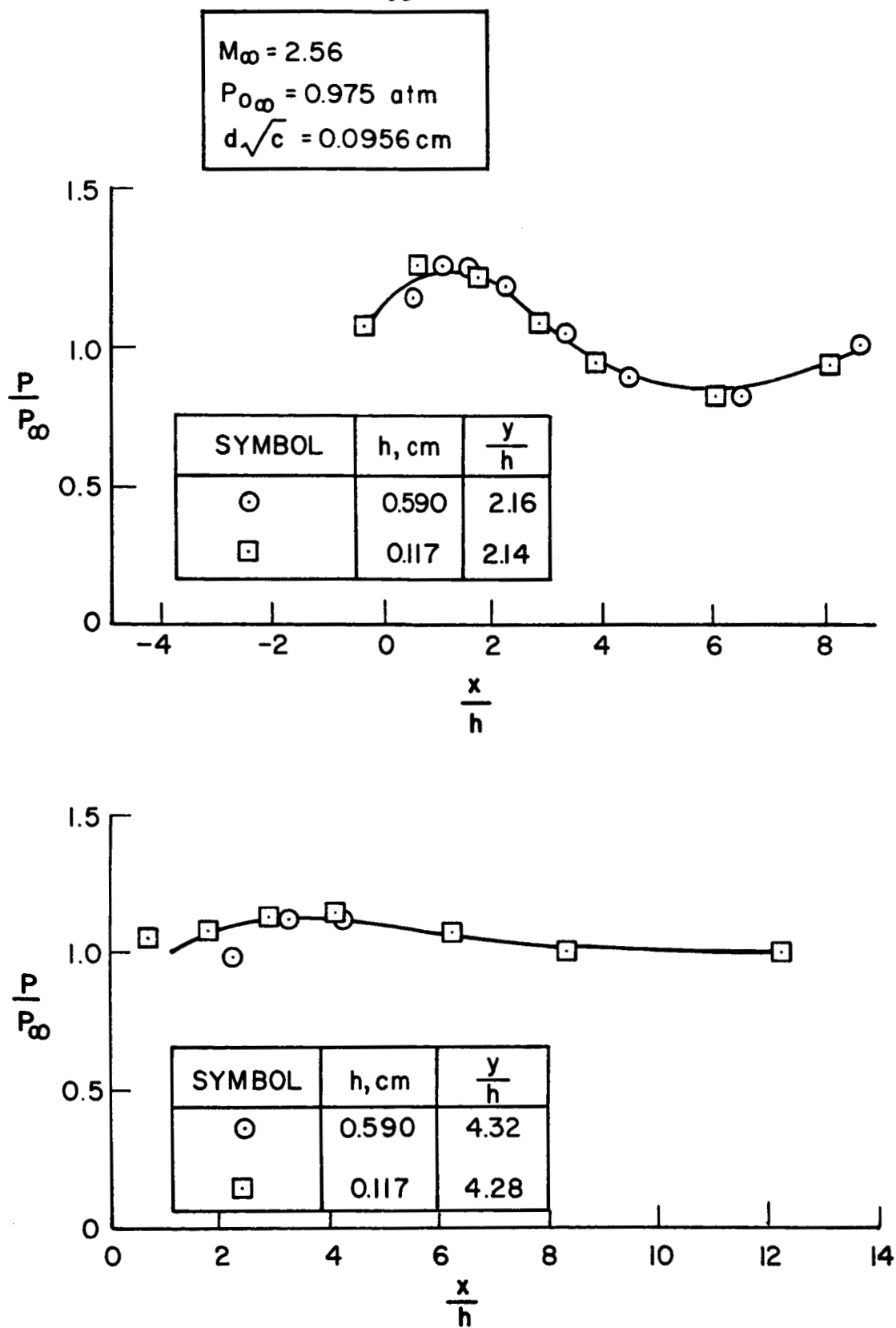


Fig.11a Nozzle-wall static pressure measurements in off-axis planes with nitrogen injection, $(y/h) = \text{constant}$.

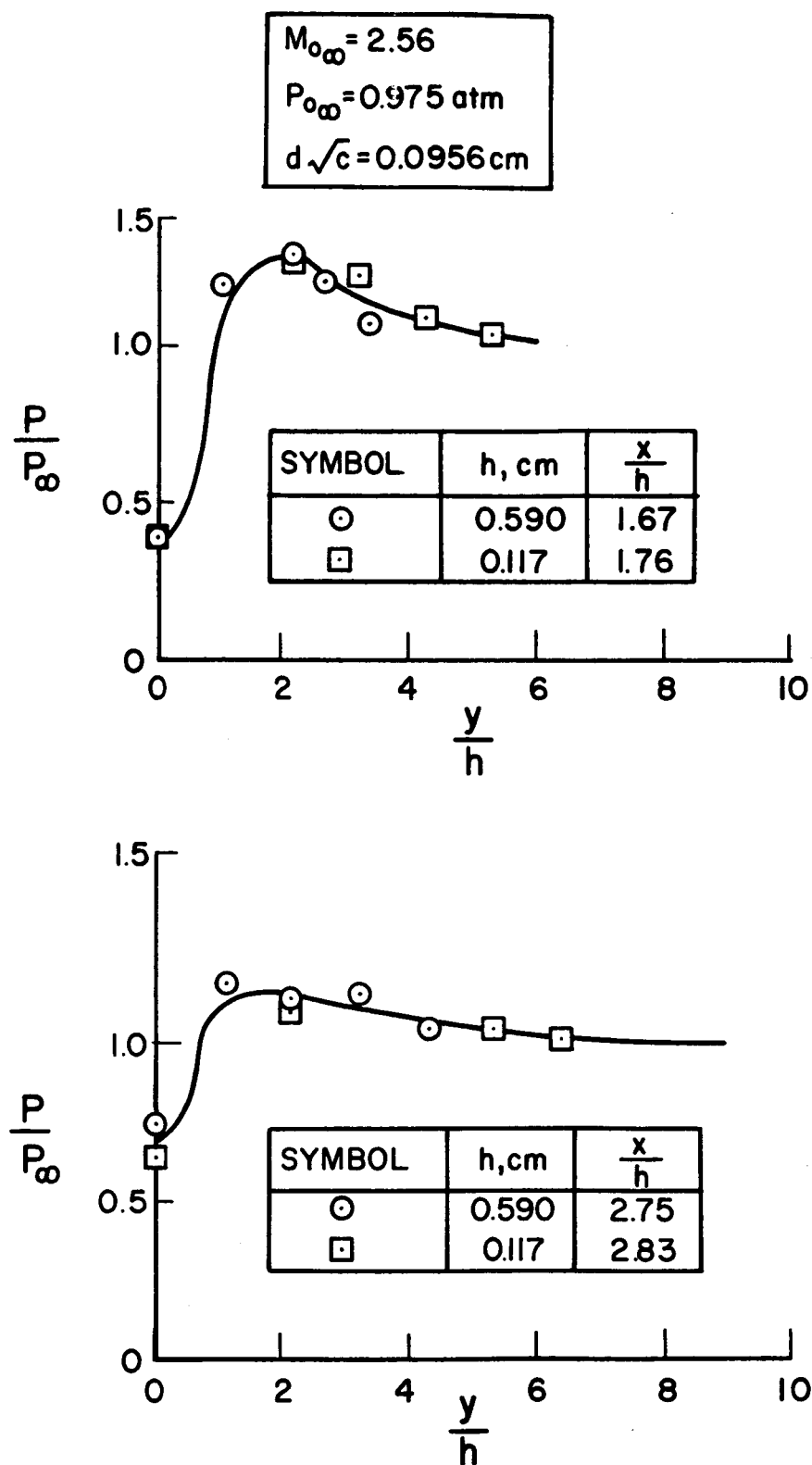


Fig. 11b Nozzle-wall static pressure measurements in off-axis planes with nitrogen injection, $(x/h) = \text{constant}$.

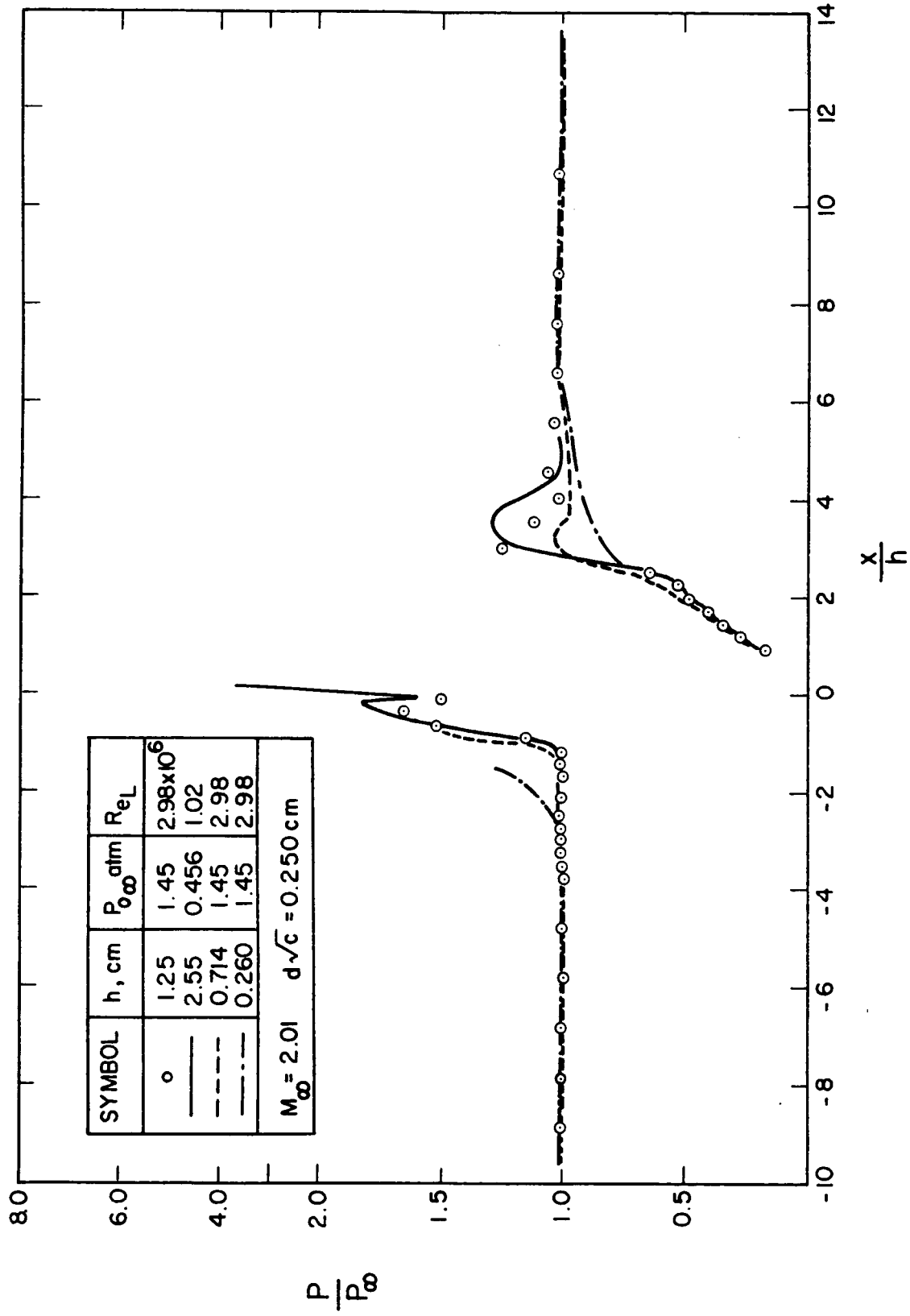


Fig.12 Flat-plate static pressure measurements in the plane $(y/h)=0$ at $M_\infty=2.01$ with nitrogen injection. Turbulent boundary layer.

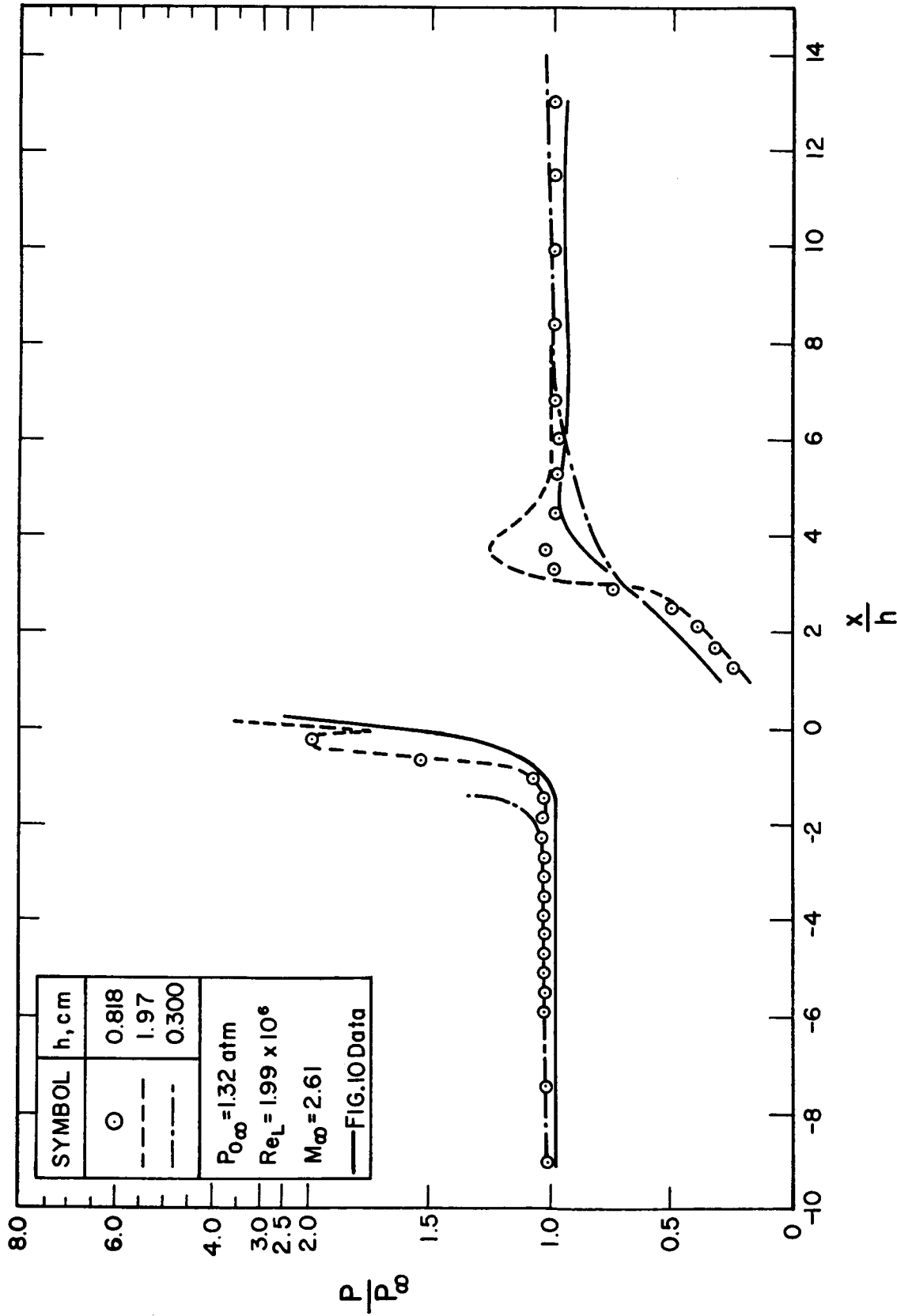


Fig. 13 Flat-plate static pressure measurements in the plane (y/h)=0 at $M_{\infty}=2.61$ with nitrogen injection. Turbulent boundary layer.

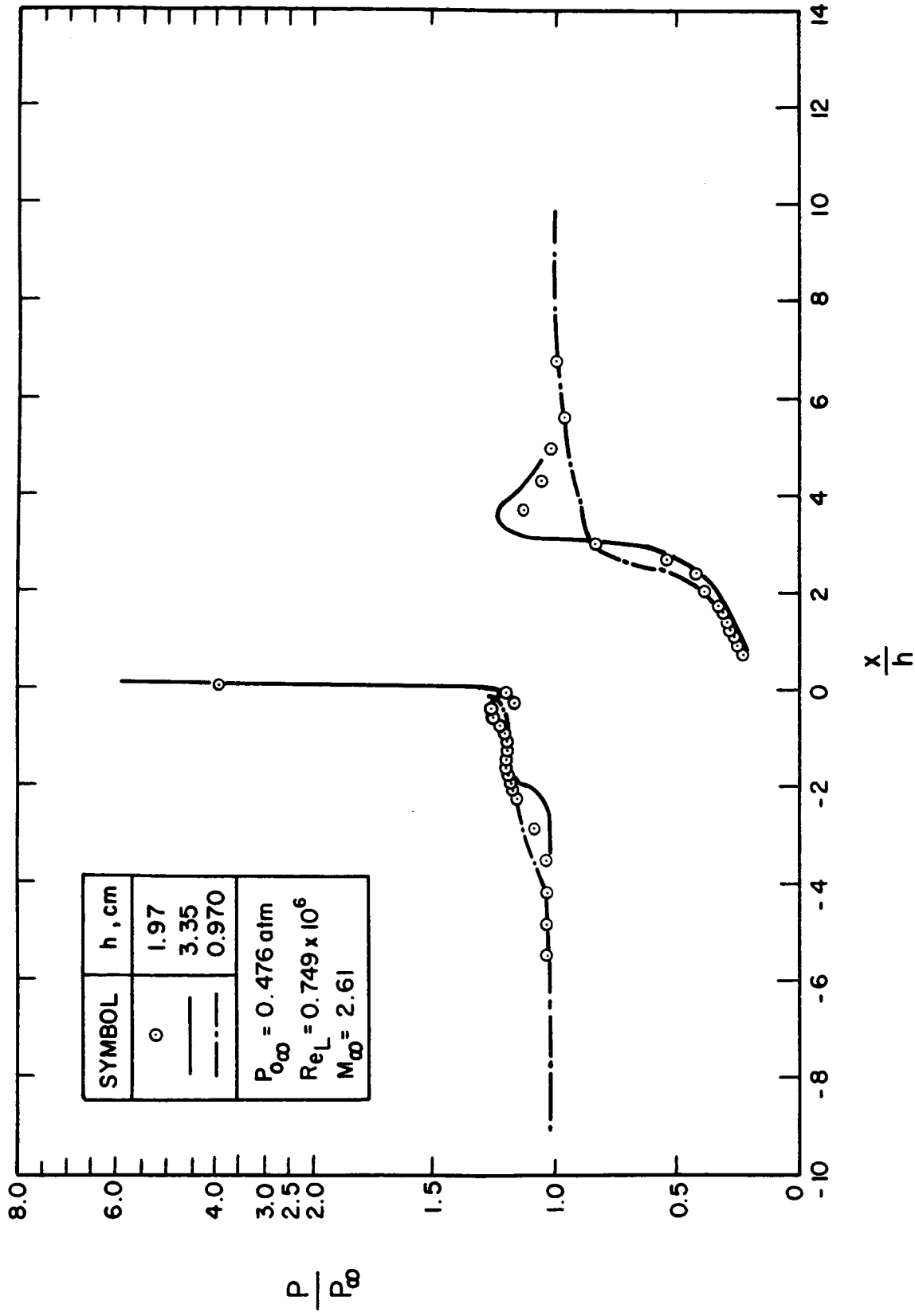


Fig. 14 Flat-plate static pressure measurements in the plane (y/h) = 0 at $M_\infty = 2.61$ with nitrogen injection. Laminar boundary layer.

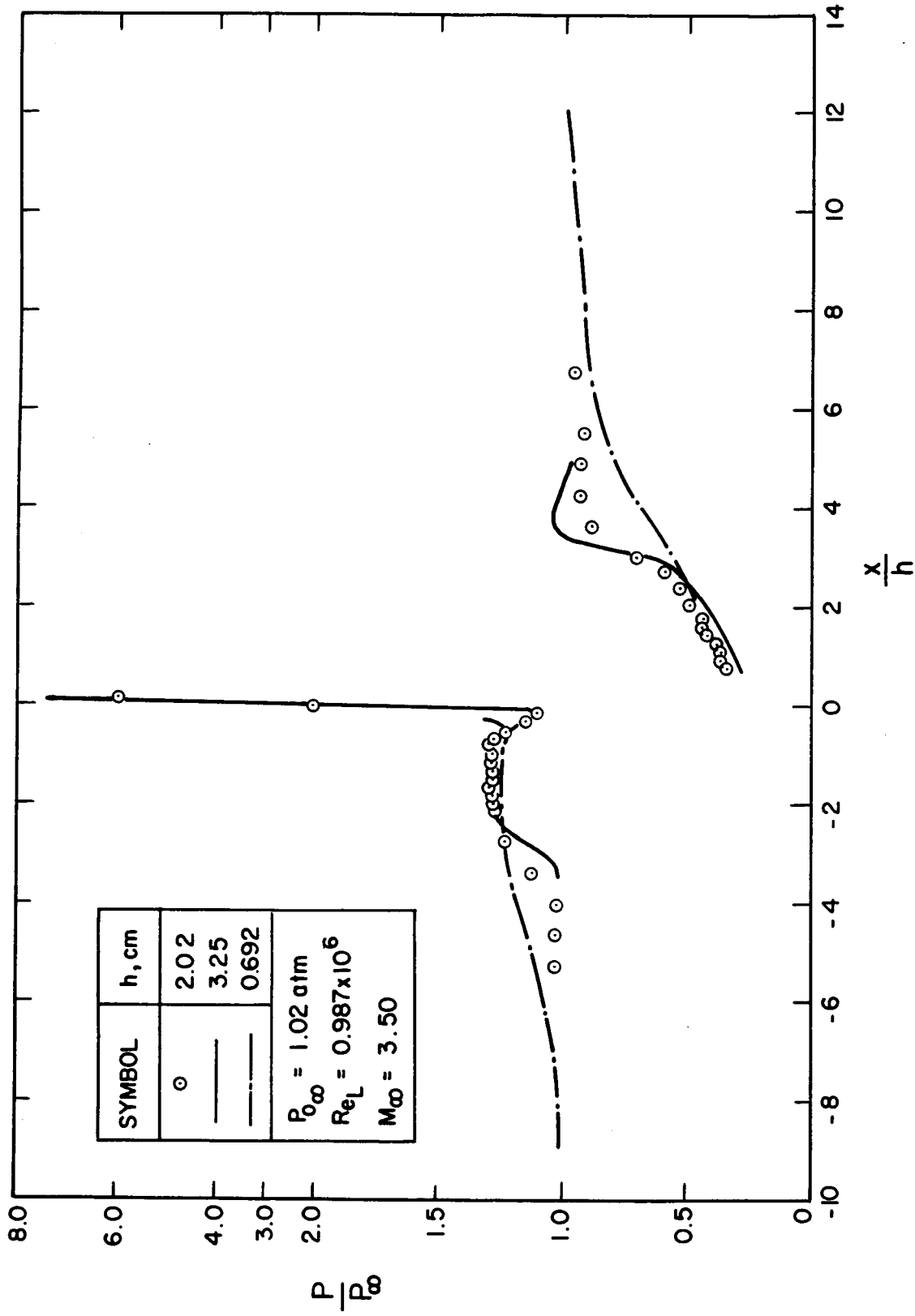


Fig. 15 Flat-plate static pressure measurements in the plane $(y/h)=0$ at $M_\infty = 3.50$ with nitrogen injection. Laminar boundary layer.

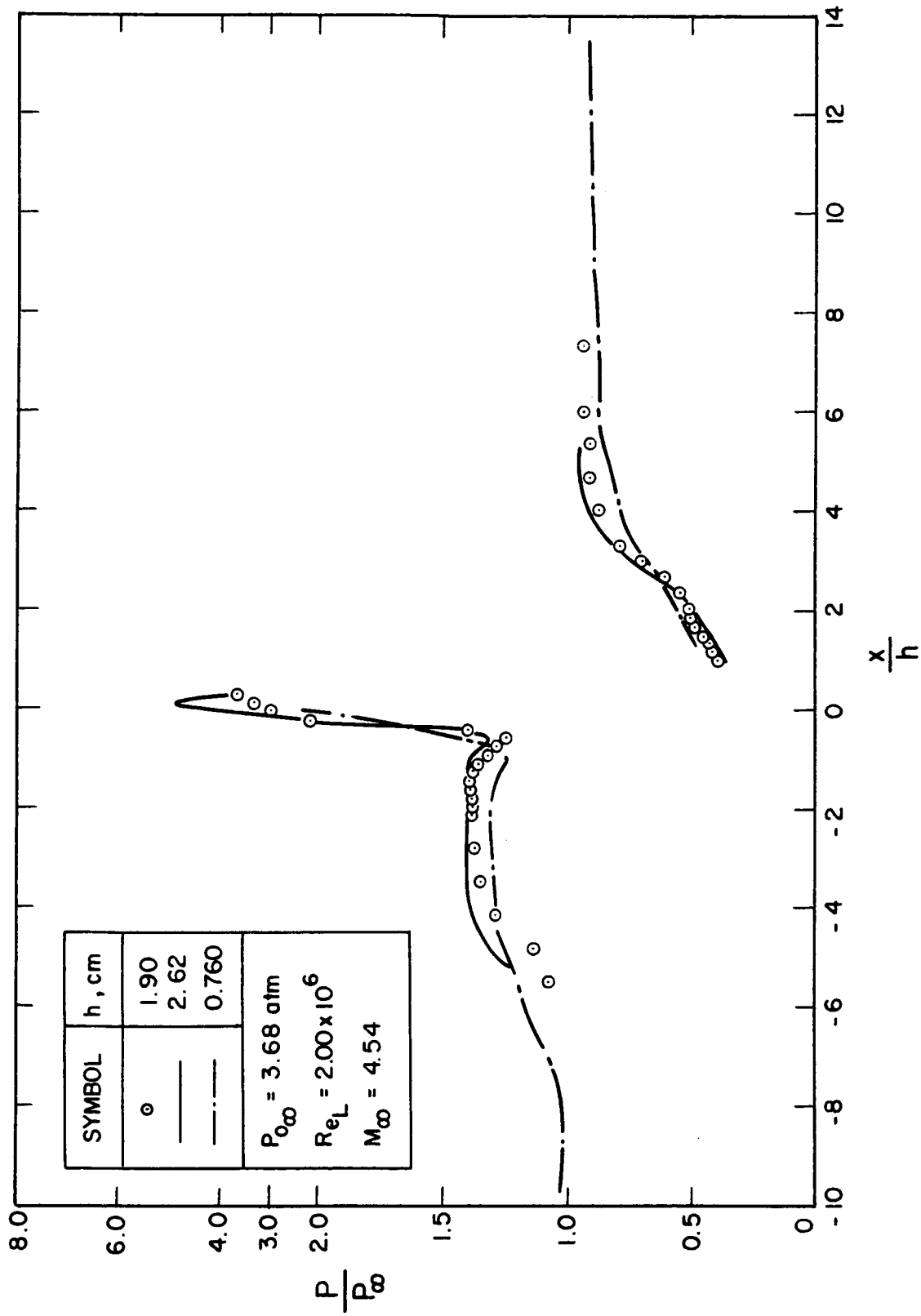


Fig.16 Flat-plate static pressure measurements in the plane $(y/h)=0$ at $M_\infty=4.54$ with nitrogen injection. Laminar boundary layer.

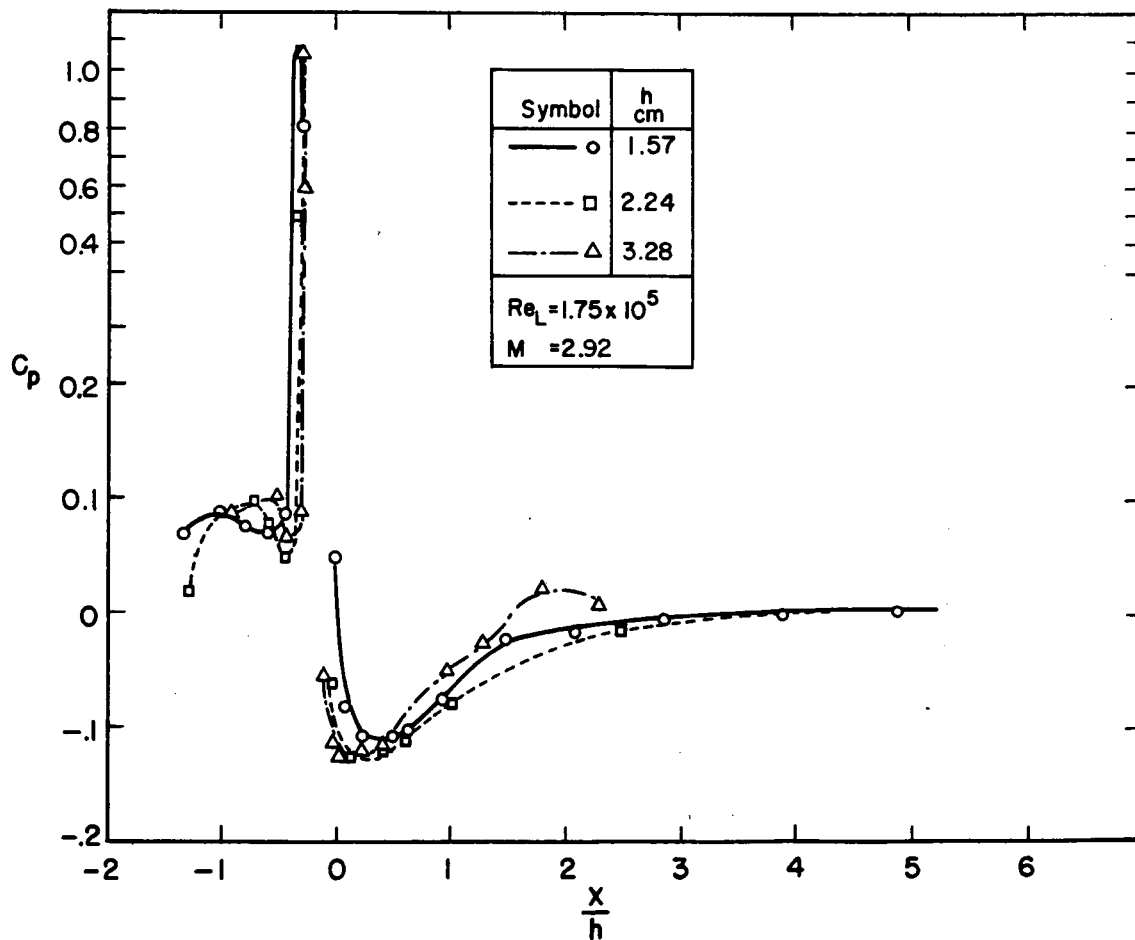
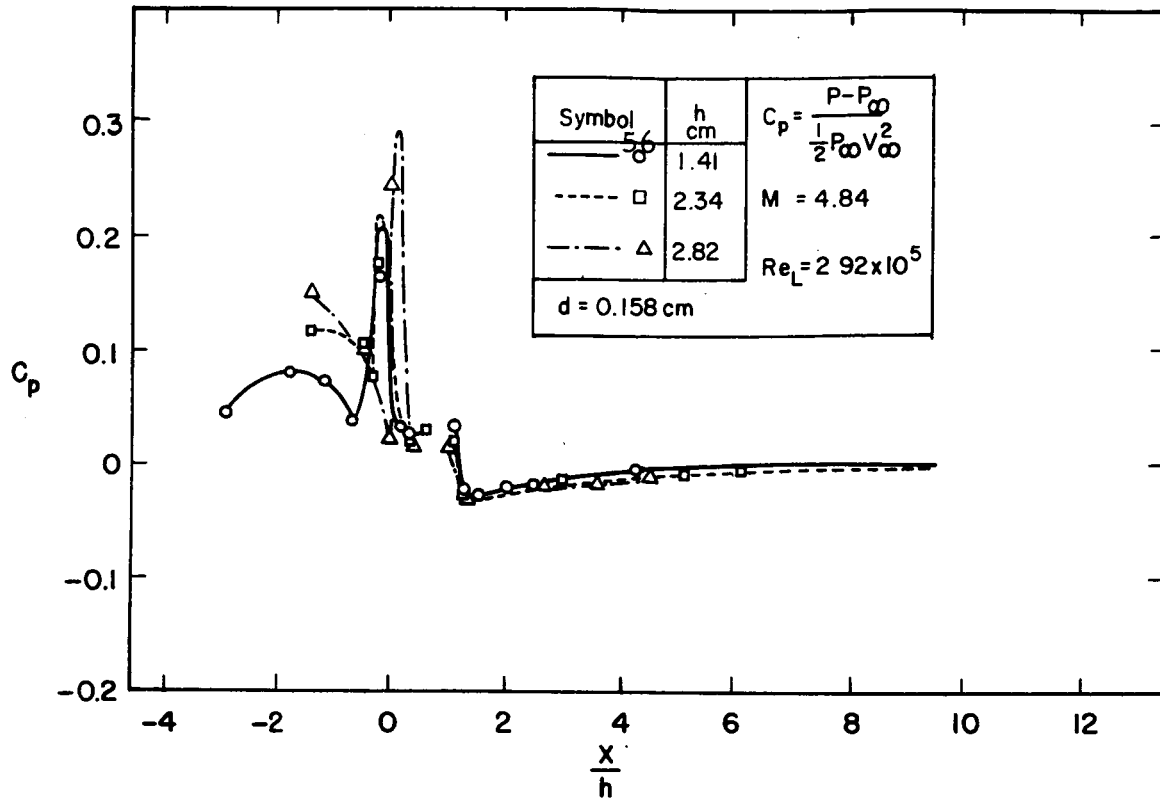


Fig.17 Correlation of pressure data from Reference 6.

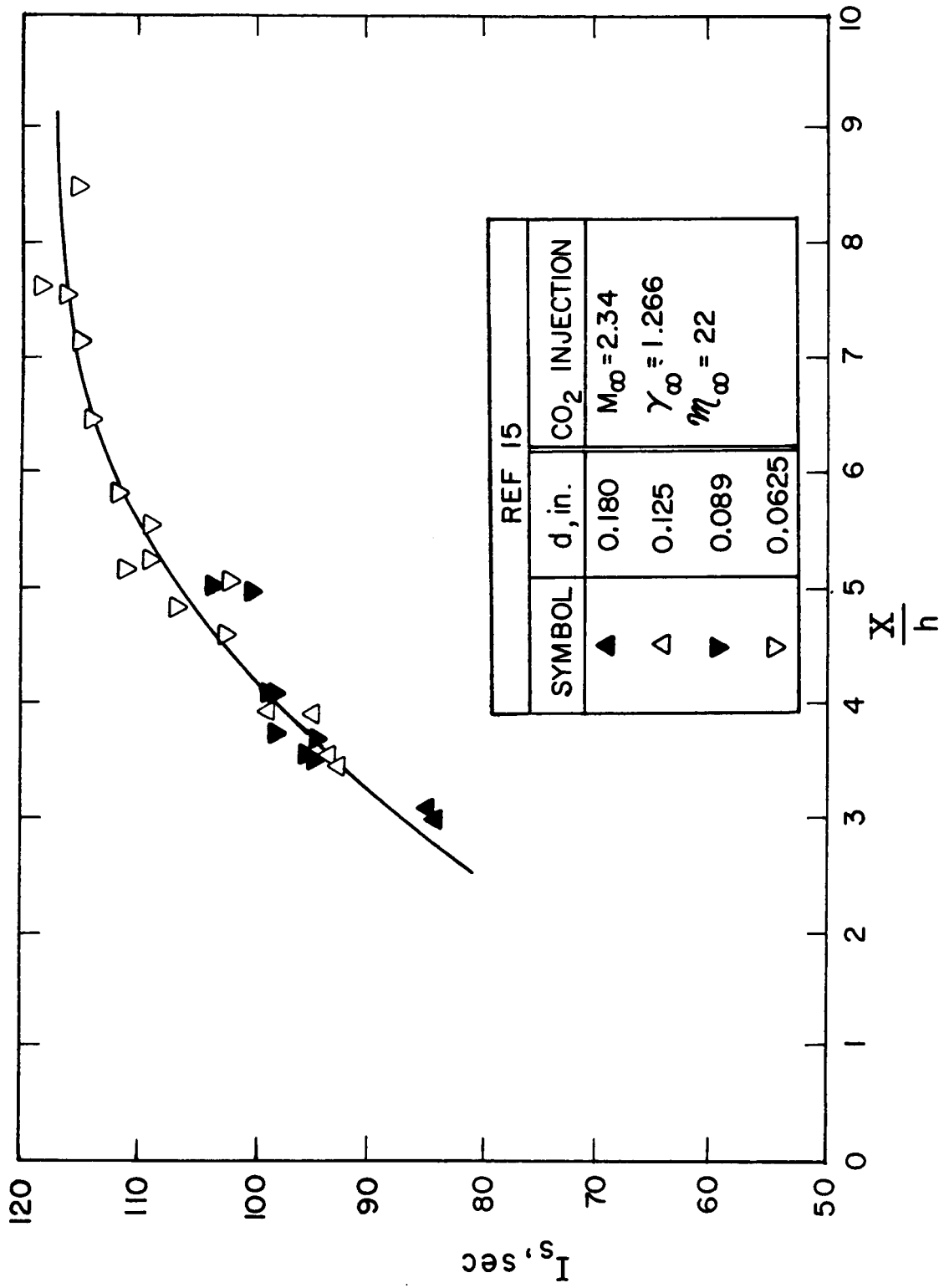


Fig.18 Variation of side specific impulse with normalized distance from injector to nozzle exit.

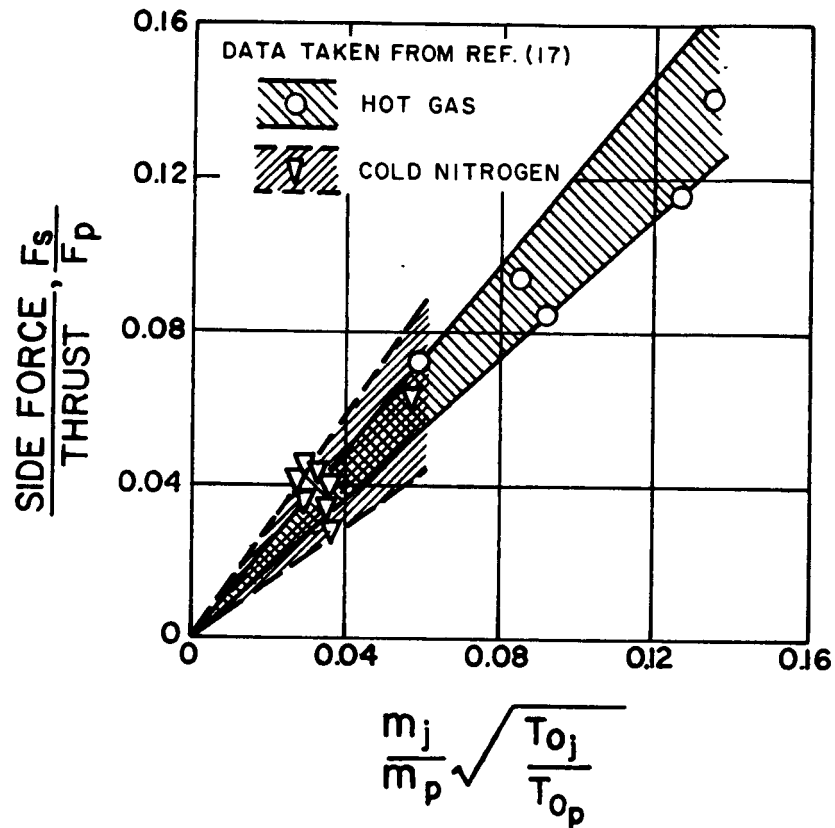


Fig. 19 Correlation of rocket-motor thrust vector-control performance for different gases and temperatures (from reference 17).

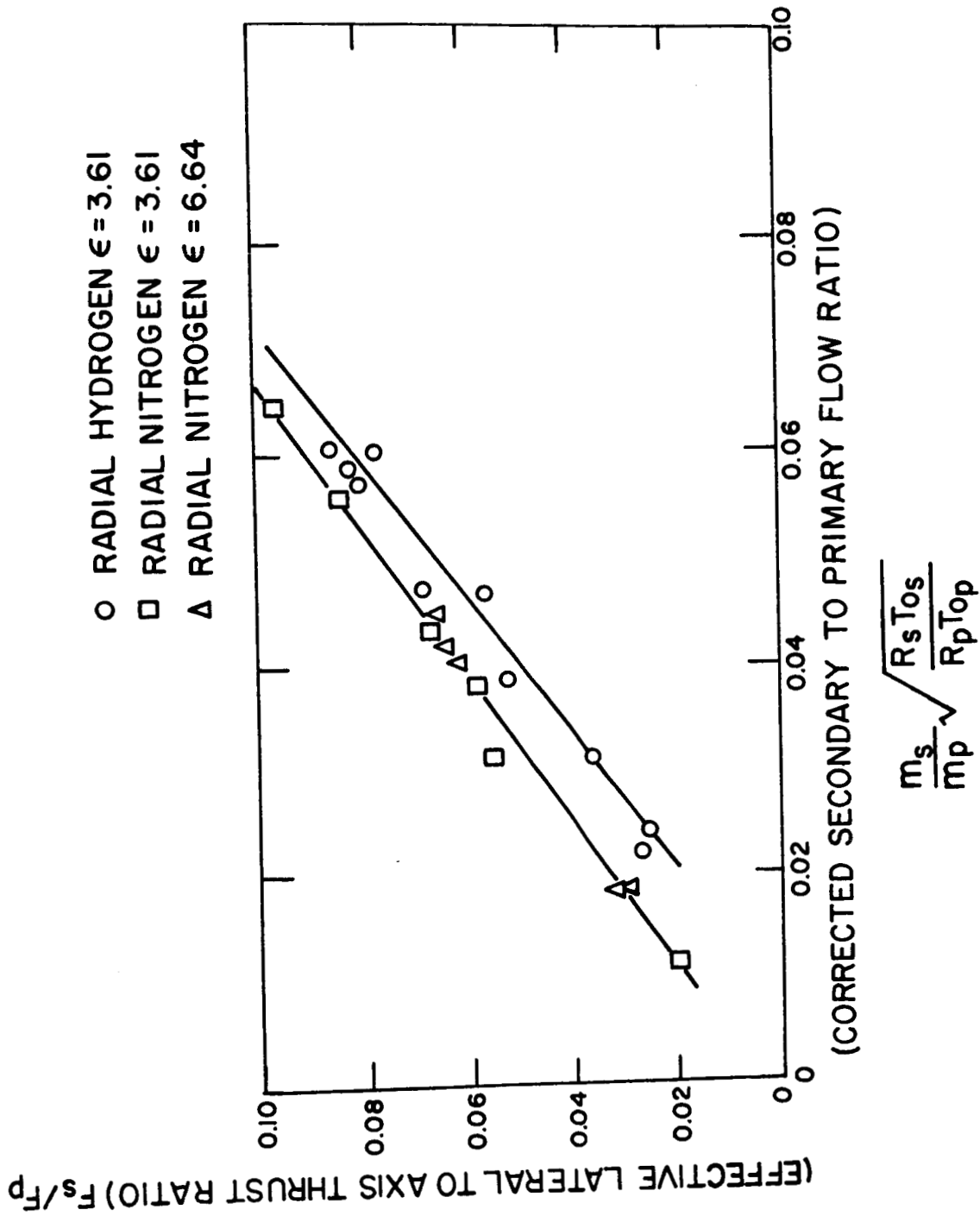


Fig.20 Correlation of rocket-motor thrust vector-control data (from reference 18).

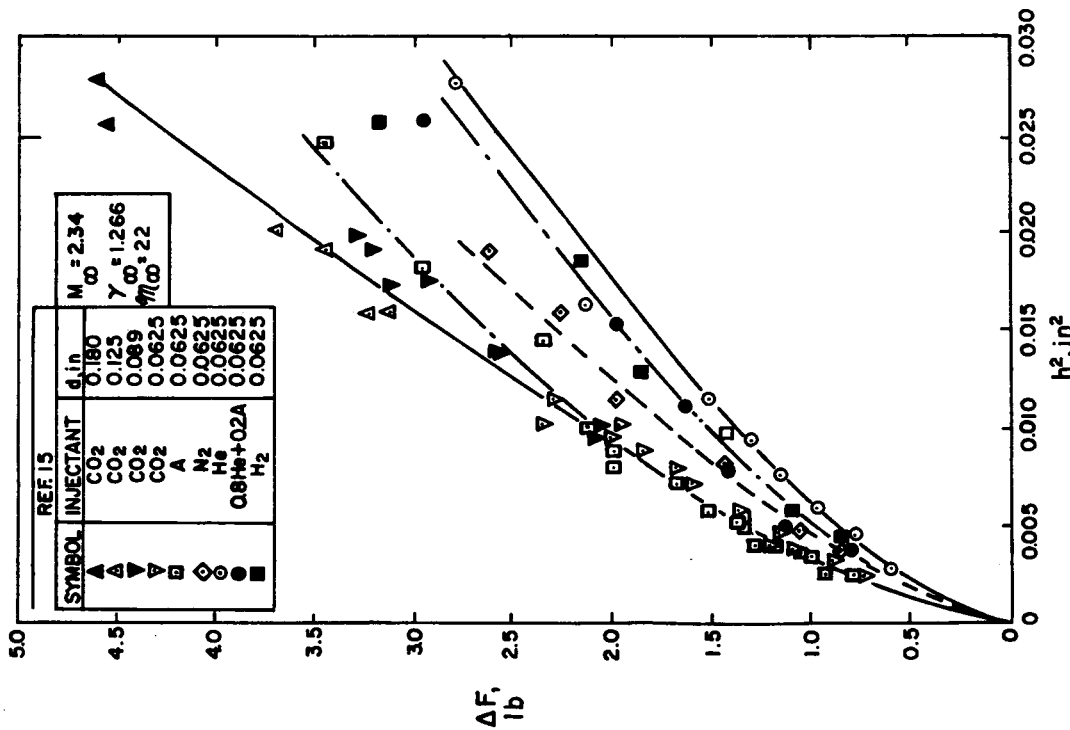


Fig. 21a Correlation of rocket-motor thrust-vector control data, (from reference 15), method of Zukoski and Spaid.

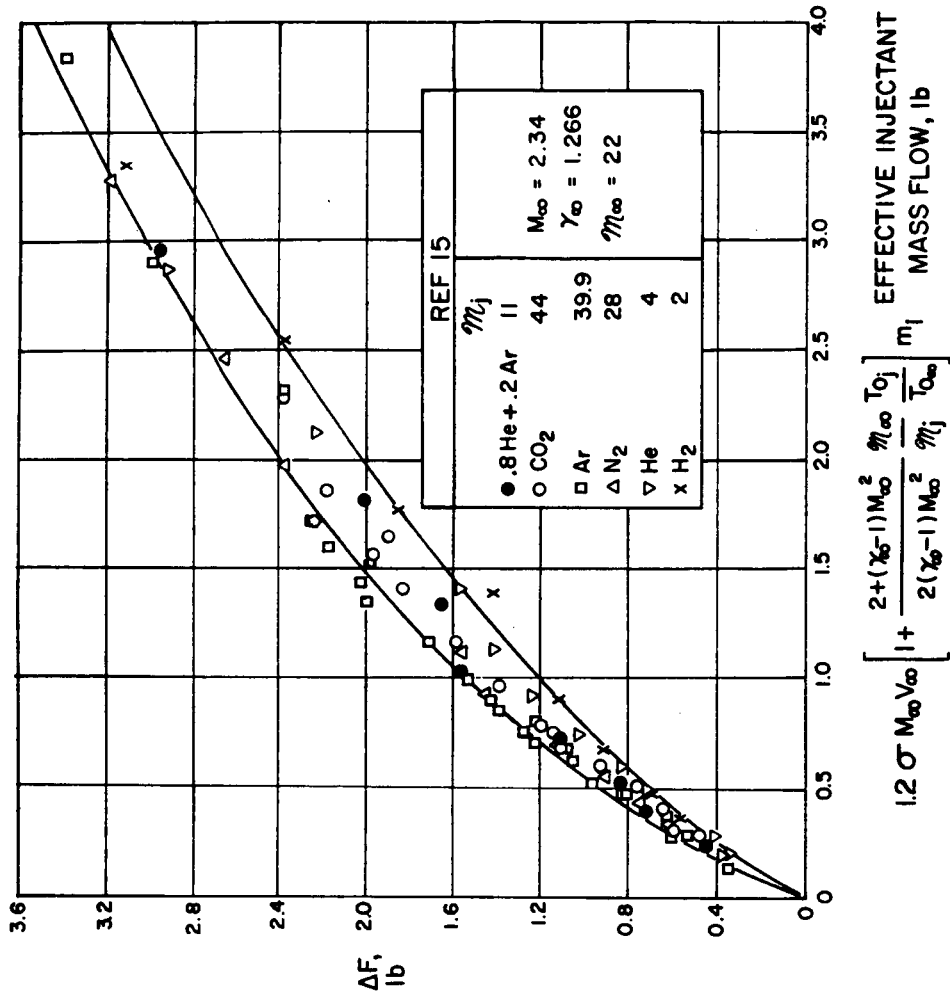


Fig. 21b Correlation of data, method of Broadwell, reference 19.